Quantum Topological Error Correction Codes Are Capable of Improving the Performance of Clifford Gates

Daryus Chandra, Zunaira Babar, Hung Viet Nguyen, Dimitrios Alanis, Panagiotis Botsinis, Soon Xin Ng, and Lajos Hanzo

***Abstract*—The employment of quantum error correction codes (QECCs) within quantum computers potentially offers a reliability improvement for both quantum computation and communications tasks. However, incorporating quantum gates for performing error correction potentially introduces more sources of quantum decoherence into the quantum computers. In this scenario, the primary challenge is to find the sufficient condition required by each of the quantum gates for beneficially employing QECCs in order to yield reliability improvements given that the quantum gates utilized by the QECCs also introduce quantum decoherence. In this treatise, we approach this problem by firstly presenting the general framework of protecting quantum gates by the amalgamation of the transversal configuration of quantum gates and quantum stabilizer codes (QSCs), which can be viewed as syndrome-based QECCs. Secondly, we provide examples of the advocated framework by invoking quantum topological error correction codes (QTECCs) for protecting both transversal Hadamard gates and CNOT gates. The simulation and analytical results explicitly show that by utilizing QTECCs, the fidelity of the quantum gates can be beneficially improved, provided that quantum gates satisfying a certain minimum depolarization fidelity threshold (F_{th}) are available. For instance, for protecting transversal Hadamard gates, the minimum fidelity values required for each of the gates in order to attain fidelity improvements are 99.74%, 99.73%, 99.87%, and 99.86%, when they are protected by colour, rotated-surface, surface, and toric codes, respectively. These specific F_{th} values are obtained for a very large number of physical qubits ($n \to \infty$), when the quantum coding rate of the QTECCs approaches zero ($r_Q \to 0$). Ultimately, the framework advocated can be beneficially exploited for employing QSCs to protect large-scale quantum computers.**

***Index Terms*—quantum error correction codes, quantum stabilizer codes, fault-tolerant, quantum topological codes, quantum gates**

I. Introduction

Quantum error correction codes (QECCs) have the potential of offering a promising reliability improvement in quantum computers. A popular member of the QECC family is constituted by quantum stabilizer codes (QSCs) [1]–[7], which can be viewed as the class of syndrome-based QECCs. The field of QECCs benefitted from a rapid pace development because under certain conditions we can transform various classes of powerful classical error correction codes into their quantum counterparts, such as Quantum Turbo Codes (QTCs) [8], [9], Quantum Low-Density Parity-Check (QLDPC) codes [10], [11], and Quantum Polar Codes (QPCs) [12], [13]. However, several challenges remain, hindering the immediate employment of these powerful QSCs in quantum computers. Firstly, the reliability of the state-of-the-art quantum gates is still significantly lower compared to classical gates. For example, the reliability of a two-qubit quantum gate is between $90.00\% - 99.90\%$ across various technology platforms, such as spin electronics, photonics, superconducting, trapped-ion, and silicon [14]–[22]. Similar to the classical domain, invoking an error correction code within a quantum computer requires an additional building block. However, adding an additional block for error correction also implies that we unavoidably introduce an additional source of decoherence into the quantum computers, since the encoder and decoder of QSCs are also composed of quantum gates. Secondly, the powerful QSCs such as QTCs, QPCs, and QLDPC codes require a very long codewords in order to operate close to the quantum hashing bound. In other words, they require a very high number of physical quantum bits (qubits) in order to correct numerous errors. Additionally, the qubits have a relatively short coherence time [23], and therefore, the error correction procedure has to be completed before the ensemble of the qubits starts decohering. Hence, utilizing QSCs having a high number of qubits for correcting many errors has the potential threat of encountering more erroneous qubits before the error correction procedure is even completed. Thirdly, the state-of-the-art architecture of quantum computers imposes an additional challenge, where the interactions among the qubits are ideally limited to the nearest neighbour qubits, which can be arranged by introducing a lattice-based topological architecture. The aforementioned challenges impose limitations on creating a fault-tolerant error correction architecture.

The quest for creating fault-tolerant gates was initialized when the notion of transversal configuration was introduced for quantum gates [24], [25]. The concept of transversal gates relies on a parallel set of identical quantum gates imposed for carrying out the operation of a single quantum gate. The fact that transversal quantum Clifford gates preserve the stabilizer formalism after the conjugation operation creates an opportunity for employing a wide range of QSCs for protecting transversal quantum gates. However, the challenges we have

The authors are with the School of Electronics and Computer Science, University of Southampton, Southampton, SO17 1BJ, UK (email: {dc2n14, zb2g10, hvn08r, da4g11, pb1y14, sxn, lh}@ecs.soton.ac.uk).

The financial support of the EPSRC under the grant EP/L018659/1, that of the European Research Council, Advanced Fellow Grant QuantCom and that of the Royal Society's Global Research Challenges Fund (GRCF) is gratefully acknowledged. Additionally, the authors acknowledge the use of the IRIDIS High Performance Computing Facility, and associated support services at the University of Southampton, in the completion of this work.

described earlier suggest that the family of quantum topological error correction codes (QTECCs) is the most suitable candidate for protecting the transversal quantum gates. The motivation behind combining the QTECCs with the transversal configuration of quantum gates is that they conveniently complement each other. More explicitly, the transversal implementation has the benefit of stabilizer preservation, while the QTECCs provide localized stabilizer measurements as detailed later in Section II, which consequently provides the benefit of a constant number of qubit interactions as we increase the number of physical qubits. Thus, the benefits provided by topologically inspired stabilizer formalism will not be affected by the transversal implementation of quantum gates. Hence, the localized action of stabilizer operators amongst the adjacent qubits, which offers fault-tolerance, is still preserved even after the desired quantum operation has been carried out by the transversal quantum gates.

However, the amalgamation of the QSCs and the transversal quantum gates can only be implemented for quantum Clifford gates, but not for the universal set of quantum gates. In order to expedite the universality of quantum computation, a set of fault-tolerant non-Clifford quantum gates has to be conceived. Fortunately, this can be achieved also using QSCs by invoking the so-called magic state distillation [26], which is however, beyond the scope of this paper. Nonetheless, the protection of Clifford gates is of significant importance, since the development of large scale quantum computers heavily relies on QSCs. This in turn hinges on the protection of quantum Clifford gates in the face of quantum decoherence.

The threshold theorem of [27] was introduced for demonstrating that a quantum computation task at a vanishingly low QBER can be carried out even with the presence of errorneous quantum gates, with the aid of QECCs as long as the error rate imposed by the quantum gates is below a certain probability value. Since the errorneous quantum gates may also result in errorneous stabilizer measurements, typically a repeated stabilizer measurements are usually required for performing the error correction. The number of stabilizer measurements required grows, as we increase the number of physial qubits utilized for QECCs. This specific problem motivated the emergence of the so-called single-shot QSCs [28]–[31]. Indeed, upon assuming that the syndrome values acquired from the syndrome mesurements are not reliable, we can still achieve a vanishingly low QBER for a quantum computation or communication task, provided that we only perform a single stabilizer masurement for each stabilizer operator. However, in order to conceive single-shot QSCs, the code constructions should satisfy certain criteria. One of them is related to the growth of the minimum distance as a function of the number of physical qubits. However, unfortunately, the quantum coding rate of the family of two-dimensional QTECCs [32]–[35] tends to zero for long codeword [36]–[38]. We also have to mention in this context that the idea of extracting reliable syndrome values from potentially error-infested stabilizer measurements is directly related to the study of the single-shot QSCs as detailed in [39]–[43]. Hence, one can ask the judicious question: "Can we still use the two-dimensional QTECCs of [32]–[35] for achieving fault-tolerant quantum computation despite relying only on a single stabilizer measurement for each of the stabilizer operators?" Arguably, the answer is yes, provided that certain conditions are satisfied. In this treatise, we answer this question by quantifying both the limit of the quantum depolarizing probability that can be tolerated by two-dimensional QTECCs and the minimum fidelity threshold required by each of the quantum gates, so that the two-dimensional QTECCs investigated can be beneficially invoked for improving the reliability of the transversal quantum gates.

Against the aforementioned background, our contributions are:

1) *We present a general framework of transversal quantum gates protected by QSCs for gate-based quantum computers by performing only a single stabilizer measurement for each of the stabilizer operators for achieving the error correction. Furthermore, we also provide a tutorial-style portrayal of this in the context of both the transversal Hadamard and controlled-NOT (CNOT) gates protected by a simple quantum repetition code.*
2) *We highlight the implementation of two-dimensional QTECCs conceived for protecting transversal Hadamard as well as CNOT gates and demonstrate the qubit error ratio (QBER) improvements attained compared to the unprotected quantum gates.*
3) *We present the upper-bound and lower-bound qubit error rate (QBER) performance of transversal quantum Clifford gates protected by QSCs.*
4) *Based on the analytical QBER performance, we found the probability threshold and the fidelity threshold to be satisfied by the quantum gates in order to obtain the benefit of reliability improvement upon employing QTECCs. These thresholds mark the ultimate limit for the physical realization of fault-tolerant quantum gates relying on QTECCs.*

The rest of this treatise is organized as follows. We provide a brief review of QTECC in Section II and then we proceed with the formulation of our framework in Section III. This is followed by the design examples of QSC-protected Hadamard and CNOT gates in Section IV, where we invoke a simple quantum repetition code as our QSC. In order to evaluate the performance of our proposed framework, in Section V, we present the decoherence model utilized in our simulations. Then in Section VI, we quantify the performance of QTECC-protected transversal Hadamard gates and CNOT gates both in terms of their QBER and fidelity along with the derivation of the QBER upper-bound and the lower-bound depolarization fidelity threshold. Finally, we conclude in Section VII.

II. Quantum Topological Error Correction Codes (QTECCs)

In order to make this treatise to be self-contained, this section provides a brief review of QSCs, more specifically QTECCs, in terms of their encoding process, stabilizer formalism, and also stabilizer measurements. In this treatise, we only present the necessary description required for understanding how the QTECCs operate. Motivated readers might like to refer to [38], [44]–[46] for more detailed information.

A. A Brief Review of Quantum Information

In the quantum domain, the fundamental unit of information is represented by the quantum bit (qubit). In contrast to the classical domain, where each of the classical bits can only carry the value of 0 or 1, a qubit can be described as a linear combination of 0 and 1, or in other words, it can be described by their superposition. However, this superposition state will collapse to the corresponding classical state of 0 or 1 upon observation or measurement. More specifically, the quantum state of a single qubit $|\psi\rangle$ can be formally expressed as

$$|\psi\rangle = \alpha_0|0\rangle + \alpha_1|1\rangle,\ \alpha_0, \alpha_1 \in \mathbb{C}, \tag{1}$$

where the probability of obtaining the classical state 0 and 1 upon measurement is given by $|\alpha_0|^2$ and $|\alpha_1|^2$, respectively. Since the values of α_0 and α_1 are associated with probability values, the unitary constraint of $|\alpha_0|^2 + |\alpha_1|^2 = 1$ is applied. A single-qubit system can also be represented as a two-dimensional Hilbert space, where the computational basis vectors $|0\rangle$ and $|1\rangle$ are defined as follows:

$$|0\rangle = \begin{pmatrix} 1 \\ 0 \end{pmatrix},\ |1\rangle = \begin{pmatrix} 0 \\ 1 \end{pmatrix}. \tag{2}$$

Therefore, the quantum state of a single qubit given in Eq. (1), can also be represented as

$$\begin{aligned} |\psi\rangle &= \alpha_0|0\rangle + \alpha_1|1\rangle \\ &= \alpha_0 \begin{pmatrix} 1 \\ 0 \end{pmatrix} + \alpha_1 \begin{pmatrix} 0 \\ 1 \end{pmatrix} \\ &= \begin{pmatrix} \alpha_0 \\ \alpha_1 \end{pmatrix},\ \alpha_0, \alpha_1 \in \mathbb{C}. \end{aligned} \tag{3}$$

Representing the basis vector of '0' using the notation $|0\rangle$ and the basis vector '1' using the notation $|1\rangle$ is referred to as the *ket* notation. The terminology *ket* comes from the *bra-ket* notation [47], where the *bra* notation refers to the $\langle\psi|$ notation, while *ket* notation is used for $|\psi\rangle$. The relationship between $|\psi\rangle$ and $\langle\psi|$ is defined as follows:

$$\langle\psi| = |\psi\rangle^\dagger, \tag{4}$$

where the notation $|\psi\rangle^\dagger$ indicates the conjugate transpose of $|\psi\rangle$. Explicitly, based on the vector representation of Eq. (3) and the definition of Eq. (4), we have

$$\langle\psi| = \begin{pmatrix} \alpha_0^* & \alpha_1^* \end{pmatrix}, \tag{5}$$

where α^* denotes the complex conjugate of α. Therefore, the following equality holds:

$$\langle\psi|\psi\rangle \equiv \langle\psi| \cdot |\psi\rangle = 1. \tag{6}$$

In general, a pair of vectors can be used as the basis vectors, as long as both of them are orthonormal, normalized and also mutually orthogonal. Apart from the above computational basis, the following Hadamard basis is also widely used in the field of QECCs:

$$|+\rangle = \frac{1}{\sqrt{2}} \begin{pmatrix} 1 \\ 1 \end{pmatrix},\ |-\rangle = \frac{1}{\sqrt{2}} \begin{pmatrix} 1 \\ -1 \end{pmatrix}. \tag{7}$$

The Hadamard basis can be viewed as the equal-weight superposition of the computational basis according to the following definition:

$$|+\rangle = \frac{|0\rangle + |1\rangle}{\sqrt{2}},\ |-\rangle = \frac{|0\rangle - |1\rangle}{\sqrt{2}}, \tag{8}$$

and vice versa. The computational basis can also be expressed as an equal-weight superposition of the vectors from the Hadamard basis, which is formulated as

$$|0\rangle = \frac{|+\rangle + |-\rangle}{\sqrt{2}},\ |1\rangle = \frac{|+\rangle - |-\rangle}{\sqrt{2}}. \tag{9}$$

In order to extend the concept of quantum information to multi-qubit systems, we have to describe the Kronecker tensor product, which is also often referred to as the tensor product. Explicitly, for a pair of matrices $\mathbf{P}$ and $\mathbf{Q}$ having $(a \times b)$ elements and $(x \times y)$ elements, respectively, the resultant tensor product is a matrix having $(ax \times by)$ elements formulated as

$$\mathbf{P} \otimes \mathbf{Q} = \begin{pmatrix} p_{11}\mathbf{Q} & \cdots & p_{1(b-1)}\mathbf{Q} & p_{1b}\mathbf{Q} \\ p_{21}\mathbf{Q} & \cdots & p_{2(b-1)}\mathbf{Q} & p_{2b}\mathbf{Q} \\ \vdots & \ddots & \vdots & \vdots \\ p_{(a-1)1}\mathbf{Q} & \cdots & p_{(a-1)(b-1)}\mathbf{Q} & p_{(a-1)b}\mathbf{Q} \\ p_{a1}\mathbf{Q} & \cdots & p_{a(b-1)}\mathbf{Q} & p_{ab}\mathbf{Q} \end{pmatrix}. \tag{10}$$

For instance, a two-qubit system is represented by the tensor product between a pair of two-element vectors given in Eq. (3). More explicitly, let us consider two qubits having the state of $|\psi_1\rangle = \alpha_0|0\rangle + \alpha_1|1\rangle$ and $|\psi_2\rangle = \beta_0|0\rangle + \beta_1|1\rangle$. The superimposed state then can be described as follows:

$$\begin{aligned} |\psi\rangle = |\psi_1\rangle \otimes |\psi_2\rangle &= \begin{pmatrix} \alpha_0 \\ \alpha_1 \end{pmatrix} \otimes \begin{pmatrix} \beta_0 \\ \beta_1 \end{pmatrix} = \begin{pmatrix} \alpha_0\beta_0 \\ \alpha_0\beta_1 \\ \alpha_1\beta_0 \\ \alpha_1\beta_1 \end{pmatrix} \\ &\equiv \alpha_0\beta_0|00\rangle + \alpha_0\beta_1|01\rangle + \alpha_1\beta_0|10\rangle + \alpha_1\beta_1|11\rangle, \end{aligned} \tag{11}$$

where $\alpha_0, \alpha_1, \beta_0, \beta_1 \in \mathbb{C}$. It can be observed that a two-qubit state is a superposition of all four possible states that can be generated by a pair of classical bits i.e. 00, 01, 10 and 11. Additionally, the unitary constraint of $|\alpha_0\beta_0|^2 + |\alpha_0\beta_1|^2 + |\alpha_1\beta_0|^2 + |\alpha_1\beta_1|^2 = 1$ still holds. The tensor product of a pair of two-element vectors yields a vector consisting of 2^2 elements. Hence, the N-qubit system produces all of 2^N possible states that can be generated by an N-bit sequence. If i is the decimal representation of an N-bit sequence, the N-qubit superposition state can be expressed by the Dirac notation as follows:

$$|\psi\rangle = \sum_{i=0}^{2^N-1} \alpha_i|i\rangle \text{ where } \alpha_i \in \mathbb{C} \text{ and } \sum_{i=0}^{2^N-1} |\alpha_i|^2 = 1. \tag{12}$$

As an instance of a very special case, where we have N qubits all having the $|+\rangle$ state provides us with all the equal-weight superposition of 2^N possible states generated by all possible combination of N-bit sequences as follows:

$$\begin{aligned} |+\rangle^{\otimes N} &\equiv |+\rangle_1 \otimes |+\rangle_2 \otimes \cdots \otimes |+\rangle_N \\ &= \frac{1}{\sqrt{2^N}} \sum_{i=0}^{2^N-1} |i\rangle, \end{aligned} \tag{13}$$

where the superscript $\otimes N$ of $|+\rangle$ represents the N-fold tensor product. It can also be observed that the probability of obtaining each of the 2^N quantum states upon measurement in the computational basis is equal to $\frac{1}{2^N}$. This particular state is often used as the initial quantum state for various quantum computing algorithms, such as Shor's quantum factoring algorithm [48], [49] and Grover's quantum search algorithm [50], [51] as well as for quantum error correction.

B. Quantum Decoherence

Quantum computers are composed by numerous quantum gates and also their interconnections, which are not immune to environmental impairments. Consequently, due to the deleterious effects of quantum decoherence, the resultant quantum state at the output may not be the desired outcome of the quantum computation. The quantum decoherence inflicting a single qubit error can be represented by the Pauli group $\mathcal{P}_1$, which defines the discrete set of possible unitary transformations imposed on a single qubit. Explicitly, the Pauli group $\mathcal{P}_1$ is defined as

$$\mathcal{P}_1 = \{eP : P \in \{\mathbf{I}, \mathbf{X}, \mathbf{Y}, \mathbf{Z}\}, e \in \{\pm 1, \pm i\}\}, \tag{14}$$

which is closed under multiplication. The unitary matrices $\mathbf{X}$ and $\mathbf{Z}$ represent the bit-flip and the phase-flip, respectively, while the matrix $\mathbf{Y}$ represents the simultaneous bit-flip and phase-flip. Finally, the identity unitary matrix $\mathbf{I}$ denotes the absence of error. These Pauli matrices are defined as follows:

$$\mathbf{I} = \begin{pmatrix} 1 & 0 \\ 0 & 1 \end{pmatrix}, \quad \mathbf{X} = \begin{pmatrix} 0 & 1 \\ 1 & 0 \end{pmatrix}, \\ \mathbf{Y} = \begin{pmatrix} 0 & -i \\ i & 0 \end{pmatrix}, \ \mathbf{Z} = \begin{pmatrix} 1 & 0 \\ 0 & -1 \end{pmatrix}. \tag{15}$$

Since the qubits whose quantum states only differ in their global phase can be deemed to be equivalent, the reduced Pauli group $\mathcal{P}_1$ denoted by $\mathcal{P}_1^*$ is often used for the sake of simulating the quantum errors by exploiting the Pauli-to-binary isomorphism [46], which is defined as

$$\mathcal{P}_1^* = \{\mathbf{I}, \mathbf{X}, \mathbf{Y}, \mathbf{Z}\}. \tag{16}$$

For the quantum state of an N-qubit system, the quantum decoherence effects may be described by the Pauli group $\mathcal{P}_n$, which is represented by an n-fold tensor product of $\mathcal{P}_1$ as defined below:

$$\mathcal{P}_n = \{P_1 \otimes P_2 \cdots \otimes P_n | P_j \in \mathcal{P}_1\}, \tag{17}$$

where the index j represents the j-th qubit of a system having n physical qubits. An operator $P \in \mathcal{P}_n$ transforms the legitimate quantum state $|\psi\rangle$ into an erroneous quantum state $|\widehat{\psi}\rangle$, as formally described below:

$$|\widehat{\psi}\rangle = P|\overline{\psi}\rangle. \tag{18}$$

The quantum decoherence may inflict an individual bit-flip ($\mathbf{X}$), a phase-flip ($\mathbf{Z}$), as well as a simultaneous bit-flip and phase-flip ($\mathbf{Y}$) error with a probability of $p^{\mathbf{X}}$, $p^{\mathbf{Z}}$, and $p^{\mathbf{Y}}$, respectively. These deleterious effects may be inflicted upon each of the qubits within the N-qubit block. Most of the literature on QSCs assume that the bit-flip, phase-flip as well as the simultaneous bit and phase-flip are equiprobable [9], [11], [44] and hence, we have $p^{\mathbf{X}} = p^{\mathbf{Z}} = p^{\mathbf{Y}} = p/3$. Consequently, the probability of having no error on an individual qubit is $p^{\mathbf{I}} = (1-p)$. This particular model is referred to as the symmetric quantum depolarizing channel.

C. Quantum Encoder

Similar to the classical domain, quantum error correction can be achieved by incorporating redundancy into the encoded word in order to maintain the level of reliability of quantum computation. In quantum domain, due to the constraints of no-cloning theorem as well as the collapsing of quantum states into classical states, the syndrome-based QECCs are widely acknowledged for mitigating the errors imposed by quantum decoherence without actually measuring the quantum information within the qubits. This specific syndrome-based QECCs are also referred to as quantum stabilizer codes (QSCs). In order to carry out the error correction task, the QSC schemes require the k logical qubits to be encoded to n physical qubits with the aid of $(n-k)$ auxiliary qubits. This specific task is carried out by the so-called quantum encoder $\mathcal{V}$. The quantum encoder $\mathcal{V}$ maps the k logical qubit based state $|\psi\rangle$ and $(n-k)$ auxiliary qubits to a unique codespace $\mathcal{C}$ of the n physical qubit based state $|\overline{\psi}\rangle$, which is defined as follows:

$$\mathcal{C} = \{|\overline{\psi}\rangle = \mathcal{V}(|\psi\rangle \otimes |0\rangle^{\otimes(n-k)})\}. \tag{19}$$

Therefore, the action of quantum encoder $\mathcal{V}$ is reminiscent of the generator matrix $\mathbf{G}$ of classical error correction codes, which have a direct relationship with the associated parity check matrix (PCM) $\mathbf{H}$ used for predicting the number and the position of errors. Similarly, in quantum domain, the function of predicting the number and the position of quantum errors is carried out by a set of stabilizer operators $S_i \in \mathcal{S}$.

Throughout this treatise, we consider gate-based quantum computation [46], [52], noting that there are many other models for quantum computation, such as measurement-based quantum computation [53], quantum cellular automata [54], topological quantum computation [55], and adiabatic quantum computation [56]. Therefore, in this treatise, we refer the readers to the method presented in [57]–[59] for creating an efficient quantum encoder $\mathcal{V}$ for QSCs. To elaborate a little further, given the so-called stabilizer operators $S_i \in \mathcal{S}$, we can transform the stabilizer operators $S_i \in \mathcal{S}$ into their classical binary PCM using the so-called Pauli-to-binary isomorphism [44], [60]. The resultant binary PCM $\mathbf{H}$ derived from the stabilizer formalism $S_i \in \mathcal{S}$ is utilized for constructing the quantum encoder $\mathcal{V}$ of the associated QECC $\mathcal{C}$. Since we deal with the family of gate-based quantum computers, naturally, the quantum encoder $\mathcal{V}$ is also composed of quantum gates.

The method specified in [57]–[59] is applicable to both Calderbank-Shor-Steane (CSS) [3]–[5] and non-CSS codes [6], [7]. However, for colour codes [34], which belong to the QTECCs family, they can also be classified further as the member of a more specific category of quantum CSS codes, namely, the dual-containing CSS codes. For dual-containing CSS codes, a specific technique can be invoked for creating the associated quantum encoder $\mathcal{V}$. This method of generating

the quantum encoder $\mathcal{V}$ of dual-containing CSS codes has been detailed in [10], [61]. It is important to note that upon using the method detailed in [10], [57]–[59], [61], the number of quantum gates required to construct a quantum encoder $\mathcal{V}$ for a QSC $\mathcal{C}$ is linearly proportional to the number of physical qubits [57], [58].

However, we can actually dispense with the quantum encoder $\mathcal{V}$ by simply preparing all the auxiliary qubits in the state of $|+\rangle$ and then perform stabilizer measurements before the transversal gates as suggested in [62], [63]. By initializing all the $(n-k)$ auxiliarry qubits to the $|+\rangle$ states, we create the equal-weight superposition of all possible combination from the $(n-k)$-bit sequences. Therefore, in order to obtain the valid encoded state of the physical qubits, we only require the stabilizer measurements for projecting the initialized space into a specific code space based on the classical bits obtained from the stabilizer measurements. This will be further elaborated further on Section IV.

D. Stabilizer Formalism

A QSC can be viewed as the a syndrome-based QECC [1], [44]. The stabilizer operator $S_i \in \mathcal{S}$ is an n-tupple Pauli operator in $\mathcal{P}_n$ preserving the legitimate encoded state of the physical qubits as encapsulated below:

$$S_i|\overline{\psi}\rangle = |\overline{\psi}\rangle. \tag{20}$$

For the erroneous physical qubits state given in Eq. (18), the action of stabilizer operators $S_i \in \mathcal{S}$ upon the state $|\widehat{\psi}\rangle$ can be formulated as follows:

$$S_i|\widehat{\psi}\rangle = \begin{cases} |\widehat{\psi}\rangle, & S_iP = PS_i \\ -|\widehat{\psi}\rangle, & S_iP = -PS_i. \end{cases} \tag{21}$$

The eigenvalues of ± 1 play the similar roles to the syndrome bits $\{1, 0\}$ of the classical error correction codes. Based on these syndrome values, an error recovery operator $R_i \in \mathcal{P}_n$ may be applied to the erroneous physical qubits. Hence, the QSC carries out its error correction procedure by predicting both the number and the position of erroneous qubits without actually measuring and altering the legitimate quantum state.

Due to the definition given in Eq. (20), stabilizer operators $S_i \in \mathcal{S}$ naturally inherit the commutative property as follows:

$$S_iS_j|\overline{\psi}\rangle = S_jS_i|\overline{\psi}\rangle = |\overline{\psi}\rangle, \forall S_{i,j} \in \mathcal{S}, i \neq j. \tag{22}$$

It also implies that the product between the stabilizer operators $S_i, S_j \in \mathcal{S}$ yields another legitimate stabilizer operator as described below:

$$S_i|\overline{\psi}\rangle = S_j|\overline{\psi}\rangle = S_iS_j|\overline{\psi}\rangle = |\overline{\psi}\rangle, \forall S_{i,j} \in \mathcal{S}, i \neq j, \tag{23}$$

suggesting that the group of stabilizer operators $\mathcal{S}$ is closed under multiplication.

Let us denote the QSC maping k logical qubits into n physical qubits having a minimum distance d as $\mathcal{C}[n, k, d]$. Hence, a QSC $\mathcal{C}[n, k, d]$ will have 2^{n-k} stabilizer operators, where all the stabilizer operators $S_i \in \mathcal{S}$ can be generated by only $(n-k)$ stabilizer generators $G_i \in \mathcal{S}$ by the multiplication between the stabilizer generators G_i. A popular family of QSCs is constituted by the QTECCs, whose constructions rely on the fact that the vertices and the plaquettes (faces) of a simple graph may be used to define their stabilizer generators. Let us refer to the rectangular lattice structure seen in Fig. 1. The physical qubits are represented by the black filled-circles located on the edges of the lattice, while the red filled-squares laying on the vertices of the graph define the $\mathbf{X}$ stabilizer generators, and finally the blue filled-triangles located on the plaquettes constitute the $\mathbf{Z}$ stabilizer generators. Formally, the stabilizer generators $G_i \in \mathcal{S}$ of the QTECCs are defined as follows:

$$A_v = \prod_{i \in \text{vertex}(v)} \mathbf{X}_i \ , \ B_p = \prod_{i \in \text{plaquette}(p)} \mathbf{Z}_i. \tag{24}$$

More specifically, the QTECC based on the rectangular lattice structure given in Fig. 1 has the stabilizer generators as portrayed in Table I[1]. One observations that we can make is that given the stabilizer generators given in Table I, all loops on the lattice structure are indeed stabilizer operators $\mathcal{S}_i \in \mathcal{S}$, since multiplying two or more stabilizers generators $G_i \in \mathcal{S}$ provide us with legitimate stabilizer operators $S_i \in \mathcal{S}$.

For a rectangular lattice exemplified in Fig. 1, we have 13 physical qubits, six $\mathbf{X}$ stabilizer operators, and six $\mathbf{Z}$ stabilizer operators. The number of logical qubits k encoded into the physical qubits n can be calculated as follows:

$$k = n - |\mathcal{G}|, \tag{25}$$

where $|\mathcal{G}|$ is the cardinality of the stabilizer generators of the stabilizer group $\mathcal{S}$. Consequently, we have a single logical qubit encoded using the specific arrangement seen in Fig. 1. The quantum coding rate r_Q of a QSC $\mathcal{C}[n, k, d]$ is defined as the ratio between the number logical qubits k to the number

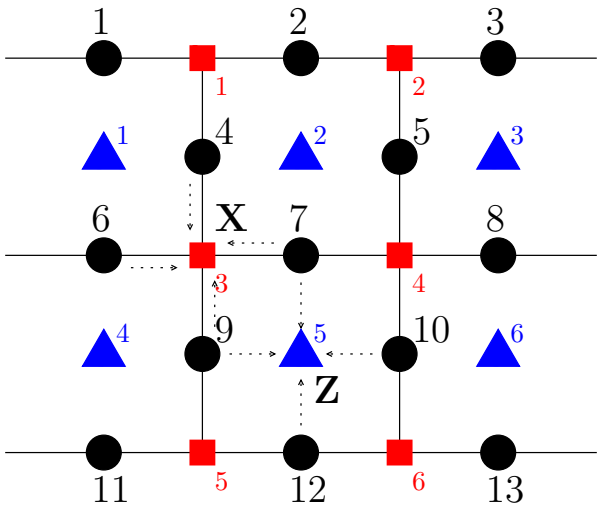

Fig. 1: An example of physical qubits arrangement on a rectangular lattice structure.

[1]In Table I, the shortened representation of stabilizer operators is used for simplifying the original representation of stabilizer operators. For example, the shortened version of $S_3 = \mathbf{X}_4\mathbf{X}_6\mathbf{X}_7\mathbf{X}_9$ is used for simplifying $S_3 = \mathbf{I}_1 \otimes \mathbf{I}_2 \otimes \mathbf{I}_3 \otimes \mathbf{X}_4 \otimes \mathbf{I}_5 \otimes \mathbf{X}_6 \otimes \mathbf{X}_7 \otimes \mathbf{I}_8 \otimes \mathbf{X}_9 \otimes \mathbf{I}_{10} \otimes \mathbf{I}_{11} \otimes \mathbf{I}_{12} \otimes \mathbf{I}_{13}$. For the rest of the paper, we always use the original representation for stabilizer operators, unless it is stated otherwise.

TABLE I: The stabilizer generators (G_i) for QSCs based on rectangular lattice structure depicted in Fig. 1. This specific construction maps a single logical qubit into 13 physical qubits. The code has a minimum distance of 3 ($d = 3$), which means that it is capable of correcting a single qubit error.

G_i	A_v	G_i	B_p
G_1	$\mathbf{X}_1\mathbf{X}_2\mathbf{X}_4$	G_7	$\mathbf{Z}_1\mathbf{Z}_4\mathbf{Z}_6$
G_2	$\mathbf{X}_2\mathbf{X}_3\mathbf{X}_5$	G_8	$\mathbf{Z}_2\mathbf{Z}_4\mathbf{Z}_5\mathbf{Z}_7$
G_3	$\mathbf{X}_4\mathbf{X}_6\mathbf{X}_7\mathbf{X}_9$	G_9	$\mathbf{Z}_3\mathbf{Z}_5\mathbf{Z}_8$
G_4	$\mathbf{X}_5\mathbf{X}_7\mathbf{X}_8\mathbf{X}_{10}$	G_{10}	$\mathbf{Z}_6\mathbf{Z}_9\mathbf{Z}_{11}$
G_5	$\mathbf{X}_9\mathbf{X}_{11}\mathbf{X}_{12}$	G_{11}	$\mathbf{Z}_7\mathbf{Z}_9\mathbf{Z}_{10}\mathbf{Z}_{12}$
G_6	$\mathbf{X}_{10}\mathbf{X}_{12}\mathbf{X}_{13}$	G_{12}	$\mathbf{Z}_8\mathbf{Z}_{10}\mathbf{Z}_{13}$

of physical qubits n, which can be expressed as follows [5]:

$$r_Q = \frac{k}{n}. \tag{26}$$

In general, QSCs will suffer from having a lower coding rate than their classical counterparts, since QSCs have to correct not only bit-flip ($\mathbf{X}$) errors, which is also the type of error experienced in classical domain, but also the phase-flip ($\mathbf{Z}$) errors as well as simultaneous bit-flip and phase-flip ($\mathbf{Y}$) errors [38], [60].

The error correction capability t of a QSC $\mathcal{C}[n, k, d]$ can be determined by its minimum distance d as follows:

$$t = \left\lfloor \frac{d-1}{2} \right\rfloor. \tag{27}$$

Therefore, in order to verify the error correction capability of a QSC $\mathcal{C}$, first we have to evaluate the minimum distance d based on the stabilizer operators $S_i \in \mathcal{S}$. Let the normalizer $\mathcal{N}(\mathcal{S}) \in \mathcal{P}_n$ be represented by the set of operators $P_i \in \mathcal{P}_n$, so that $PS_iP^\dagger = S_j \in \mathcal{S}$ for all $S_i \in \mathcal{S}$ and i is not necessarily equal to j. It is plausible that all the stabilizer operators $S_i \in \mathcal{S}$ are automatically in $\mathcal{N}(\mathcal{S})$. Now, we are interested in the specific set of operators in the normalizer $\mathcal{N}(\mathcal{S})$ that does not belong to the stabilizer operators $\mathcal{S}$, which is denoted by $\mathcal{N}(\mathcal{S}) - \mathcal{S}$. The minimum distance of a QSC $\mathcal{C}$ is equal to d, if and only if $\mathcal{N}(\mathcal{S}) - \mathcal{S}$ contains no elements with weight less than d, where the weight of a Pauli operator $P_i \in \mathcal{P}_n$ is given by the number of non-identity Pauli operators. In other words, the minimum distance of a QSC $\mathcal{C}$ can be defined by the minimum weight of the operators P_i, which commutes with all stabilizer operators $S_i \in \mathcal{S}$, but it is not an element of $\mathcal{S}$.

In case of the rectangular lattice structure of Fig. 1, a good example of such an operator P_i is constituted by the chains connecting the two boundaries of the lattice. To elaborate a little further, let us consider a Pauli operator P represented by the shortened version $P = \mathbf{X}_2\mathbf{X}_7\mathbf{X}_{12}$ connecting the boundaries of the lattice of Fig. 1. It can be readily checked that this specific Pauli operator P commutes with all the stabilizer generators $G_i \in \mathcal{S}$, but it cannot be represented as the product of any stabilizer generators $G_i \in \mathcal{S}$. Since P_i represents the lowest-weight Pauli operator P_i commuting with all the stabilizer operators $S_i \in \mathcal{S}$, but not an element of $\mathcal{S}$, the weight of P_i determines the minimum distance of the QSC defined by the rectangular lattice of Fig. 1. Therefore, we conclude that based on the stabilizer generators given in Table I, the minimum distance of the QSC defined by the rectangular lattice of Fig. 1 is $d = 3$. Furthermore, the size of the lattices defining the stabilizer operators $G_i \in \mathcal{S}$ can be used for calculating the minimum distance d, the number of logical qubits and physical qubits, as well as the quantum coding rate r_Q. More details on this topic are provided in [38].

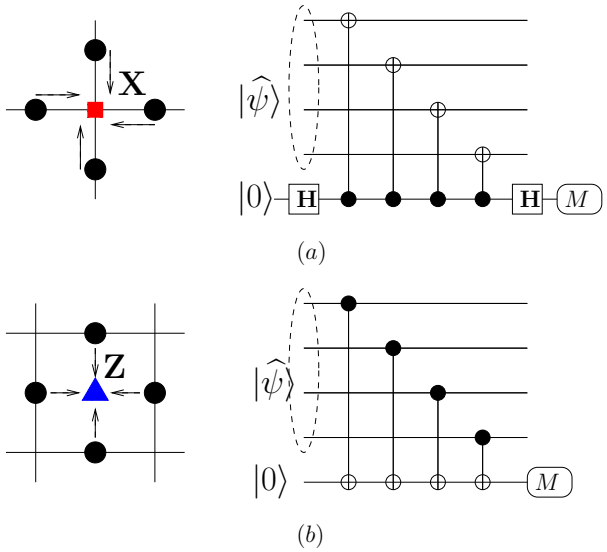

Fig. 2: Stabilizer measurements for QTECCs based on rectangular lattice depicted in Fig. 1. (a) The $\mathbf{X}$ stabilizer measurement. (b) The $\mathbf{Z}$ stabilizer measurement.

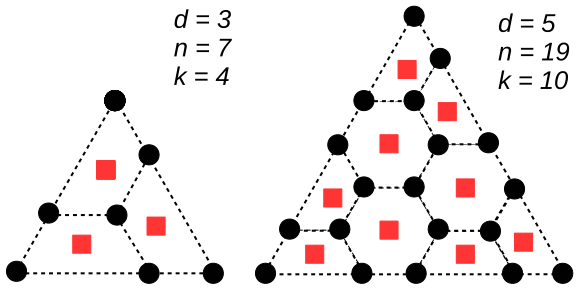

Fig. 3: An example of qubit arrangements in colour codes. The black circles on the vertices represent the physical qubits, while the red squares on the plaquettes constitute both the $\mathbf{X}$ and $\mathbf{Z}$ stabilizer operators.

Since the stabilizer operators of QTECCs are defined based on the underlying lattice structure, the stabilizer measurement can be performed locally in the lattice, i. e. without invoking more distant qubits in the lattice. The $\mathbf{X}$ and $\mathbf{Z}$ stabilizer measurements of the rectangular lattice structure given in Fig. 1 are portrayed in Fig. 2. It can be clearly observed that due to the constraints imposed by the lattice structure, each of the physical qubits will have to interact with at most two $\mathbf{X}$ stabilizer measurements and two $\mathbf{Z}$ stabilizer measurements.

The QTECCs defined over square lattice structure exemplified in Fig. 1 are referred to as surface codes [33]. However, the square lattice is not the only structure defining the stabilizer formalism of QTECCs. Another example is colour codes [34], where the stabilizer generators $G_i \in \mathcal{S}$ are defined over triangular and hexagonal lattice structures as depicted in Fig. 3. In Fig. 3, the physical qubits are represented by the black circles on the vertices of the lattice, while the stabilizer measurements are represented by the red squares on the plaquette. The main difference is that the plaquette of the lattice is used for defining both $\mathbf{X}$ and $\mathbf{Z}$ stabilizer operators. Furthermore, we can observe that each physical qubit only interacts with at most three stabilizer measurements and this number will remain constant even for a larger lattice dimension. This property is quite important in this treatise, since we want to keep the number of interacting qubits as low as possible. In this treatise, for the sake of comparison, we will use four types of QTECCs, namely surface codes [33], colour codes [34], rotated-surface codes [35], and toric codes [32].

III. Protecting Transversal Gates

In this section, we present the design of QSC-protected quantum gates along with the pivotal theory in quantum information processing required for formulating the proposed framework.

A. Quantum Clifford Gates

The quantum gates manipulating the state of the qubits are represented using the unitary transformation U, which satisfies

$$U^\dagger U = \mathbf{I}. \tag{28}$$

Since the quantum gates themselves also potentially impose the deleterious effect of quantum decoherence, which is represented by the Pauli group $\mathcal{P}_n$, the evolution of quantum decoherence through the quantum gates can be described using the conjugation of the unitary transformation.

Let us assume that a unitary transformation of M is applied to a quantum state of $N|\psi\rangle$, where N is also a unitary transformation that has been applied previously. Therefore, the final quantum state is given by $MN|\psi\rangle$. Since M is a unitary transformation, thus we have $M^\dagger M = \mathbf{I}$. The quantum state of $MN|\psi\rangle$ can be transformed as follows:

$$\begin{aligned} MN|\psi\rangle &= MNM^\dagger M|\psi\rangle \\ &= VM|\psi\rangle, \end{aligned} \tag{29}$$

where we have $V = MNM^\dagger$, which is the conjugate of N under the unitary transformation M. Consequently, Eq. (29) implies that the unitary transformation $MNM^\dagger$ after the operator M acts similarly to the unitary transformation N before the operator M. For instance, a Hadamard gate is defined by a unitary matrix as follows:

$$\mathbf{H} = \frac{1}{\sqrt{2}} \begin{pmatrix} 1 & 1 \\ 1 & -1 \end{pmatrix}. \tag{30}$$

The transformation carried out by the Hadamard gates map the quantum state in computational basis into the Hadamard basis, as described below:

$$\begin{aligned} \mathbf{H}|0\rangle &= \frac{|0\rangle + |1\rangle}{\sqrt{2}} \equiv |+\rangle, \\ \mathbf{H}|1\rangle &= \frac{|0\rangle - |1\rangle}{\sqrt{2}} \equiv |-\rangle \end{aligned} \tag{31}$$

and vice versa. Based on the conjugation of Eq. (29), we arrive at the following transformations:

$$\begin{aligned} \mathbf{HXH}^\dagger &= \mathbf{Z}, \\ \mathbf{HZH}^\dagger &= \mathbf{X}, \\ \mathbf{HYH}^\dagger &= -\mathbf{Y}. \end{aligned} \tag{32}$$

One way to interpret the transformation given in Eq. (32) is that a bit-flip $(\mathbf{X})$ error before the Hadamard gate is equivalent to a phase-flip $(\mathbf{Z})$ error after the Hadamard gate. Similarly, a phase-flip $(\mathbf{Z})$ error before the Hadamard gate can be treated as an $\mathbf{X}$ error after the Hadamard gate. Another example is the phase gate $(\mathbf{S})$, which is defined by the unitary transformation of

$$\mathbf{S} = \begin{pmatrix} 1 & 0 \\ 0 & i \end{pmatrix}. \tag{33}$$

Based on Eq. (29) and on the unitary matrix of $\mathbf{S}$ in Eq. (33), we arrive at the following transformations:

$$\begin{aligned} \mathbf{SXS}^\dagger &= \mathbf{Y} \\ \mathbf{SZS}^\dagger &= \mathbf{Z} \\ \mathbf{SYS}^\dagger &= -\mathbf{X} \end{aligned} \tag{34}$$

Moreover, the relationship given in Eq. (29) can also be adopted to the model of the conjugation over two-qubit quantum gates. An example of two-qubit quantum gate is CNOT, whose unitary transformation is defined by the following unitary matrix:

$$\mathbf{CNOT} = \begin{pmatrix} 1 & 0 & 0 & 0 \\ 0 & 1 & 0 & 0 \\ 0 & 0 & 0 & 1 \\ 0 & 0 & 1 & 0 \end{pmatrix}. \tag{35}$$

A CNOT gate is a two-qubit quantum gate, where the first qubit is called control qubit and the second qubit is referred to as target qubit. The value of target qubit is flipped if and only if the value of control qubit is equal to one. Based on Eq. (29), the two-qubit conjugation over the CNOT gate can be readily formulated as follows:

$$\begin{aligned} (\mathbf{CNOT})(\mathbf{X} \otimes \mathbf{I})(\mathbf{CNOT})^\dagger &= \mathbf{X} \otimes \mathbf{X}, \\ (\mathbf{CNOT})(\mathbf{I} \otimes \mathbf{X})(\mathbf{CNOT})^\dagger &= \mathbf{I} \otimes \mathbf{X}, \\ (\mathbf{CNOT})(\mathbf{Z} \otimes \mathbf{I})(\mathbf{CNOT})^\dagger &= \mathbf{Z} \otimes \mathbf{I}, \\ (\mathbf{CNOT})(\mathbf{I} \otimes \mathbf{Z})(\mathbf{CNOT})^\dagger &= \mathbf{Z} \otimes \mathbf{Z}. \end{aligned} \tag{36}$$

We can also interpret the result as an error transformation or an error propagation process, illustrated in Fig. 4. It can be observed that a bit-flip or $\mathbf{X}$-type error imposed on the control qubit before the CNOT gate will propagate to the target qubit after the CNOT gate. Meanwhile, a $\mathbf{Z}$-type error inflicted upon

the target qubit before the CNOT gate will impose another **Z**-type error on the control qubit after the CNOT gate.

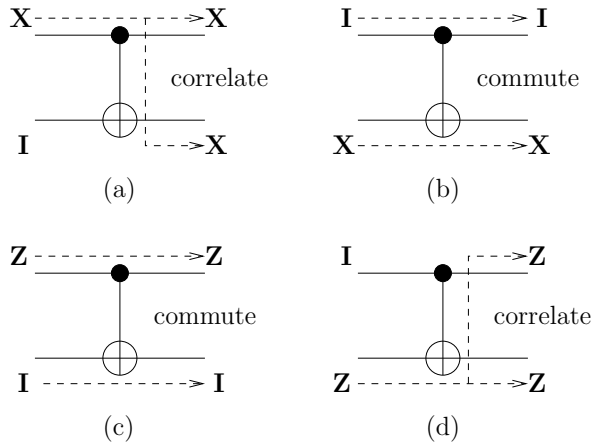

Fig. 4: The evolution of two-qubit unitary transformation over the CNOT quantum gate, which is the circuit level interpretation of Eq. (36). For example, an **X**-type error imposed on the control qubit will propagate to the target qubit after the CNOT gate, as we can observe in (a). By contrast, a **Z**-type error inflicting the target qubit will propagate to the control qubit after the CNOT gate, which is shown in (d).

In this treatise, we limit our discussions to quantum gates belonging to the Clifford group, since the stabilizer formalism of QTECCs will be preserved under conjugation [64], [65]. The theory of protecting quantum circuits using QSCs has been widely investigated [24], [25], [66]–[70] and in this treatise, we provide a comparative study of the quantum circuits protected by QSCs, specifically by the family of QTECCs. The most reasonable way of embedding QSCs into quantum gates is by the transversal implementation of quantum gates. The physical interpretation of the transversal implementation of QTECCs, specifically that of CNOT gates, is illustrated in Fig. 5. In the physical implementation, we can imagine having a pair of lattice structures arranged on a wafer, where each of the physical qubit layers is encoded using a QTECC scheme. The first qubit from the upper layer acts as the control qubit, while the first qubit from the lower layer serves as the target qubit. It is followed by the second, the third, and all the remaining physical qubits from the upper as well as the lower layer.

B. Design Formulation

The employment of QSCs for protecting the quantum circuits indeed increases the reliability of quantum computing, as shown in [61]. However, in order to avoid a perpetual encoding and decoding process throughout the quantum circuit before the number of errors exceeds the error correction capability of the QSC, we present a more efficient framework, where we encode the logical qubits at the input of the quantum circuit and decode them afterwards at the output of the computational step. However, the unitary transformation U_f applied to the state of physical qubits alters the legitimate state of physical qubits. Therefore, the initial stabilizer operators $S_i \in \mathcal{S}$ designed for stabilizing the legitimate state of physical qubits are no longer valid after the application of the unitary transformation U_f. Fortunately, we are able to conceive an *effective stabilizer formalism* and *effective inverse encoder* for successfully circumventing the problem[2].

To elaborate a little further, let us observe the basic model for QSC portrayed of Fig. 6(a) and the basic scheme of protecting quantum gates using QSC, as depicted in Fig. 6(b). We would like to highlight the main differences between the conventional QSC scheme of Fig. 6(a) and the QSC scheme conceived for protecting the quantum gates shown in Fig. 6(b). Firstly, in Fig. 6(a), the stabilizer operators $S_i \in \mathcal{S}$ are designed for stabilizing the state of physical qubits $|\overline{\psi}\rangle$, while the effective stabilizer operators $\widehat{S}_i \in \widehat{\mathcal{S}}$ in Fig. 6(b) are constructed for stabilizing the state of physical qubits after the unitary transformation $U_f|\overline{\psi}\rangle = |\overline{\psi_2}\rangle$. Consequently, the recovery procedures of $R_i \in \mathcal{R}$ based on stabilizer operators $\mathcal{S}$ is also modified according to the effective stabilizer operators $\widehat{\mathcal{S}}$ into the effective recovery operators $\widehat{R}_i \in \widehat{\mathcal{R}}$. Secondly, the inverse encoder $\mathcal{V}^\dagger$ of Fig. 6(a) is designed to recover the original state of the logical qubit $|\psi\rangle$, while in Fig. 6(b), the block $\widehat{\mathcal{V}}^\dagger$ is invoked for restoring the state of the logical qubits $|\overline{\psi_0}\rangle$, which has been transformed by the unitary transformation U_f into $U_f|\overline{\psi_0}\rangle$.

Now, we proceed to specifically elaborate further on the scheme proposed for protecting quantum gates using QSCs, as shown in Fig. 6(b). Let us commence with the logical qubits in the state of $|\psi\rangle$ representing the input of the quantum circuit. In order to encode the logical qubits, we require $(n-k)$ auxiliary qubits (ancillas) all in the state of $|0\rangle$. We assume that fresh ancillas are always available provided by a quantum memory. Hence, the state of the logical qubits and of the ancillas can be expressed as

$$|\overline{\psi_0}\rangle = |\psi\rangle \otimes |0\rangle^{\otimes(n-k)}. \tag{37}$$

The quantum encoder $\mathcal{V}$ of Fig. 6(b) maps the input state of $|\overline{\psi_0}\rangle$ into the state of encoded logical qubits or physical qubits $|\overline{\psi_1}\rangle$ as follows:

$$|\overline{\psi_1}\rangle = \mathcal{V}|\overline{\psi_0}\rangle. \tag{38}$$

The unitary operation U_f of Fig 6(b), which is the unitary transformation that we wish to protect, maps the physical qubits in the state of $|\overline{\psi_1}\rangle$ onto $|\overline{\psi_2}\rangle$ as follows:

$$|\overline{\psi_2}\rangle = U_f|\overline{\psi_1}\rangle = U_f\mathcal{V}|\overline{\psi_0}\rangle. \tag{39}$$

It is important to note that the unitary transformation of U_f may impose quantum errors $\mathcal{P}$ on the encoded state $|\overline{\psi_2}\rangle$, as it will be shown later in Section V.

Due to the unitary tranformation U_f of Fig. 6(b) after the quantum encoder $\mathcal{V}$, the stabilizer operators of $S_i \in \mathcal{S}$ are no longer applicable to the encoded state of $|\overline{\psi_2}\rangle$, because the stabilizer formalism $\mathcal{S}$ was designed for stabilizing the encoded state of $|\overline{\psi_1}\rangle$. Since the aim of this scheme is to protect the state

[2]The term *effective* means that the stabilizer formalism and the inverse encoder at the output of computational step takes into account both the initial stabilizer formalism and quantum encoder when we encode the logical qubits at the input and the unitary transformation applied upon the input physical qubits.

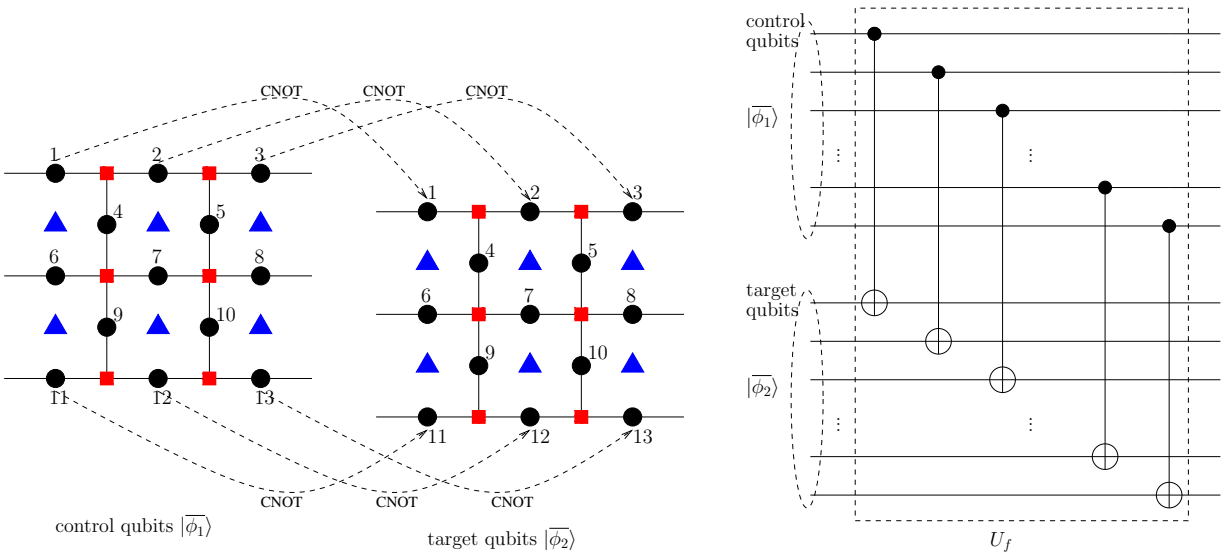

(a) (b)

Fig. 5: The physical interpretation of the transversal CNOT gates is portrayed in (a), while (b) depicts its interpretation at the circuit level. In the physical implementation of (a), we can imagine two layers of physical qubits, where on each layer the physical qubits are arranged over a lattice structure portrayed in Fig. 1. The CNOT interactions are performed accordingly on each of the pairs of physical qubits. The CNOT interactions between the physical qubits number #4 to #10 are removed from the figure for the sake of avoiding obfuscation. The physical layout portrayed in (a) can be translated into circuit level interpretation of (b), where it represents a chain of CNOT gates.

of $|\overline{\psi_2}\rangle$ instead of $|\overline{\psi_1}\rangle$, a different stabilizer formalism, which we refer to as the effective stabilizer operators $\widehat{S}_i \in \widehat{\mathcal{S}}$, should be designed for stabilizing the state of $|\overline{\psi_2}\rangle$ by taking into account the unitary transformation U_f. Given the formulation in Eq. (29), we represent the effective stabilizer operator $\widehat{S}$ as follows:

$$\begin{aligned} |\overline{\psi_2}\rangle &= U_f|\overline{\psi_1}\rangle \\ &= U_f S|\overline{\psi_1}\rangle \\ &= U_f S U_f^\dagger U_f|\overline{\psi_1}\rangle \\ &= \widehat{S}U_f|\overline{\psi_1}\rangle \\ &= \widehat{S}|\overline{\psi_2}\rangle, \end{aligned} \tag{40}$$

where $\widehat{S}$ is the effective stabilizer for $|\overline{\psi_2}\rangle$, which is defined by

$$\widehat{S} = U_f S U_f^\dagger, \tag{41}$$

for stabilizing the state of $|\overline{\psi_2}\rangle$ in Fig. 6(b).

Given a unitary function U_f and a set of stabilizer operators $S_i \in \mathcal{S}$, there are three possible outcomes due to the effective stabilizer formalism of Eq. (41). Firstly, the set of stabilizer operators does not change ($\widehat{\mathcal{S}} = \mathcal{S}$). In other words, the overall stabilizer operators are preserved. This specific result arises because the unitary transformation U_f is constituted by certain types of transversal quantum Clifford gates, such as for instance transversal Hadamard gates or CNOT gates and because $S_i \in \mathcal{S}$ belongs to the family of dual-containing CSS-type QSCs. Secondly, the stabilizer operators are changed ($\widehat{\mathcal{S}} \neq \mathcal{S}$). One of the possible reasons that we arrive at the second result is because we apply the QSCs to non-transversal quantum Clifford gates. Since the stabilizer operators are changed, there is a chance that the resultant stabilizer operators $\widehat{S}_i \in \widehat{\mathcal{S}}$ are associated with a QSC exhibiting a higher error correction capability. This is reminiscent of the idea of code deformation presented in [71]–[74]. Defining U_f for the non-transversal configurations of the quantum Clifford gates in order to achieve an increased error correction capability constitutes a substantial open research question on its own right. Hence, we set aside this issue for our future research. Thirdly, the resultant set of stabilizer operators $\widehat{S}_i \in \widehat{\mathcal{S}}$ constitutes no longer a set of n-tupple Pauli operators. This means that the unitary transformation U_f is not represented by a Clifford quantum gate. More specifically, if the unitary transformation U_f is represented, for example, by a Tofolli gate [46], our QSCs cannot be directly invoked for protecting the quantum gates by the procedures presented in this treatise. In order to tackle this problem, magic state distillation as a technique required for protecting non-Clifford quantum gates was proposed in [26]. Again, in this treatise, we focus our attention on the first possible outcome, since we are dealing with transversal quantum Clifford gates. Nevertheless, the aforementioned remaining implications of the effective stabilizer formalism are also interesting research directions.

Next, after performing the stabilizer measurements of $\widehat{S}_i \in \widehat{\mathcal{S}}$, the error recovery procedure $\widehat{\mathcal{R}}$ of Fig. 6(b) acts according to the effective stabilizer measurements and we obtain the predicted legitimate physical qubits state of $|\widehat{\psi_2}\rangle$. The final task of our system given in Fig. 6(b) is to perform a unitary transformation in order to transform the final state of $|\widehat{\psi_2}\rangle$ into the state of $U_f|\overline{\psi_0}\rangle$. Similar to the stabilizer formalism $\mathcal{S}$ in Fig. 6(a), the inverse encoder $\mathcal{V}$ was also designed

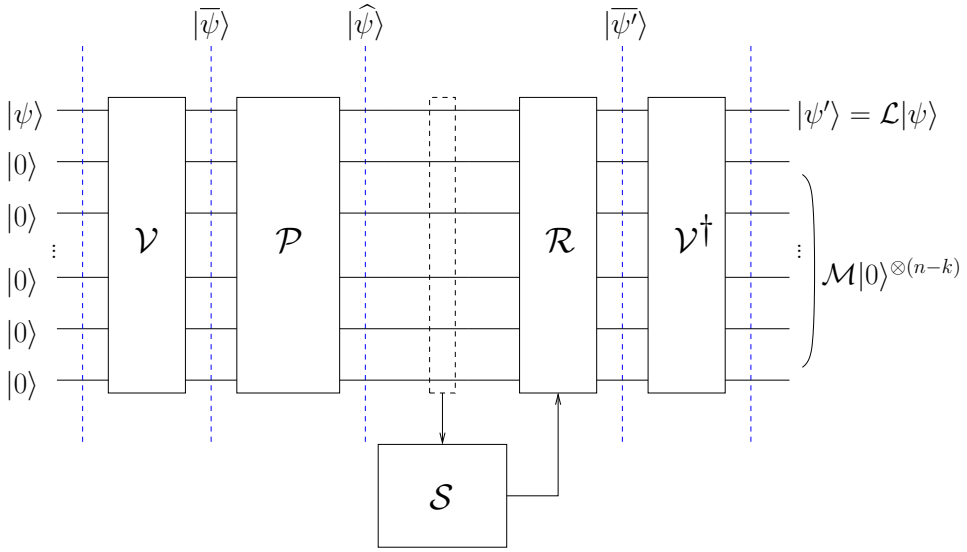

(a) The basic model of QSCs implementation over the quantum depolarizing channel.

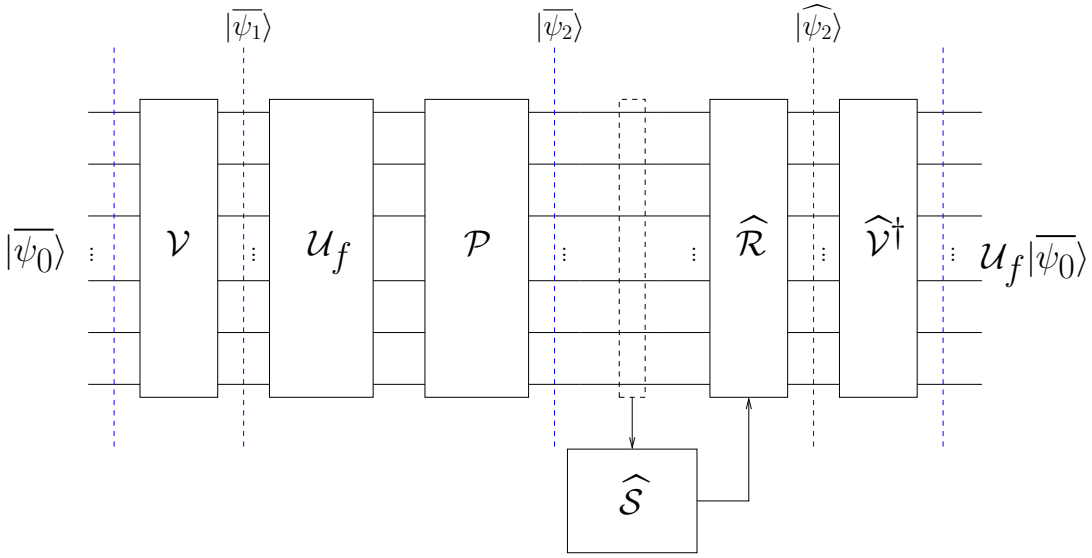

(b) The basic model for QSC-protected quantum gates where the unitary transformation $\mathcal{U}_f$ introduces quantum depolarizing channel.

Fig. 6: The comparison between QSC for correcting the errors imposed by quantum channel $\mathcal{P}$ without and with unitary transformation $\mathcal{U}_f$. Figure (a) depicts the standard scheme for protecting the encoded state of physical qubits $|\overline{\psi}\rangle$. In this scheme, the purpose of applying a QSC is to recover the state of logical qubit $|\psi\rangle$ by stabilizing the state $|\overline{\psi}\rangle$ using the stabilizer operators $S_i \in \mathcal{S}$ in the presence of depolarizing channel $\mathcal{P}$. Figure (b) portrays the modified scheme for protecting the encoded state of physical qubits $|\overline{\psi_2}\rangle$, which is the encoded state after unitary transformation $\mathcal{U}_f$. In this scheme, instead of stabilizing the state of $|\overline{\psi_1}\rangle$, the stabilizer operators have to stabilize the state of $|\overline{\psi_2}\rangle$. Since the stabilizer operator $S_i \in \mathcal{S}$ is only valid for the encoded state of $|\overline{\psi_1}\rangle$, we have to reformulate the stabilizer operators S_i for stabilizing the encoded state $|\overline{\psi_2}\rangle$, which we refer to as the *effective stabilizer operators* $\widehat{S}_1 \in \widehat{\mathcal{S}}$.

for recovering the state of $|\overline{\psi}_1\rangle$, which is based on the stabilizer formalism $\mathcal{S}$. Therefore, we require the *effective inverse encoder* $\widehat{\mathcal{V}}^\dagger$, which is designed based on the effective stabilizer operators $\widehat{\mathcal{S}}$, as seen in Fig. 6(b), to recover the state of $U_f|\overline{\psi_0}\rangle$. The formulation used for describing the effective inverse encoder $\widehat{\mathcal{V}}^\dagger$ is given by

$$\begin{aligned} U_f|\overline{\psi_0}\rangle &= U_f \left(U_f\mathcal{V}\right)^\dagger \left(U_f\mathcal{V}\right)|\overline{\psi_0}\rangle \\ &= U_f \left(U_f\mathcal{V}\right)^\dagger |\overline{\psi_2}\rangle \\ &= U_f\mathcal{V}^\dagger U_f^\dagger|\overline{\psi_2}\rangle \\ &= \widehat{\mathcal{V}}^\dagger|\overline{\psi_2}\rangle, \end{aligned} \tag{42}$$

where $\widehat{\mathcal{V}}^\dagger$ is the effective inverse encoder for $|\overline{\psi_2}\rangle$, which is

defined as:

$$\widehat{\mathcal{V}}^{\dagger} = U_f \mathcal{V}^{\dagger} U_f^{\dagger}. \tag{43}$$

Finally, as seen in Eq. (42), the effective inverse encoder $\widehat{\mathcal{V}}^{\dagger}$ succesfully transforms the state $|\overline{\psi_2}\rangle$ into the state of $U_f|\overline{\psi_0}\rangle$.

IV. Design Examples

One of the strategies we may rely on for creating high-reliability quantum gates is that of invoking the unitary transformation U_f, which is a sequence of quantum gates arranged in a transversal fashion. For example, let us consider a quantum gate protected by $1/3$-rate quantum repetition code as shown in Fig. 7(a). More explicitly, based on the model depicted in Fig. 6(b), we describe the transversal implementation of both the Hadamard and of the CNOT gates protected by the $1/3$-rate quantum repetition code.

A. Transversal Hadamard Gates

First, we would like to elaborate on the transversal implementation of Hadamard gates protected by a $1/3$-rate quantum repetition code. Let us refer to Fig. 7(a). The procedure begins with encoding the state of a single logical qubit $|\psi\rangle = \alpha|0\rangle + \beta|1\rangle$ and two auxiliarry qubits in the state of $|0\rangle$ into the state of physical qubits of $|\overline{\psi_1}\rangle$ with the aid of quantum encoder $\mathcal{V}$ as follows:

$$\begin{aligned} |\overline{\psi_1}\rangle &= \mathcal{V}\left(|\psi\rangle \otimes |0\rangle^{\otimes 2}\right) \\ &= \mathcal{V}\left((\alpha|0\rangle + \beta|1\rangle) \otimes |0\rangle^{\otimes 2}\right) \\ &= \alpha|000\rangle + \beta|111\rangle \\ &\equiv \alpha|0\rangle_L + \beta|1\rangle_L, \end{aligned} \tag{44}$$

where $|0\rangle_L = |000\rangle$, $|1\rangle_L = |111\rangle$, and the quantum encoder $\mathcal{V}$ for this mapping is portrayed by the part marked by $\mathcal{V}$ in Fig. 7(a). The encoded state of the physical qubits given in Eq. (44) is stabilized by the stabilizer operators generated by S_i:

$$\begin{aligned} S_1 &= \mathbf{Z}_1 \otimes \mathbf{I}_2 \otimes \mathbf{Z}_3, \\ S_2 &= \mathbf{Z}_1 \otimes \mathbf{Z}_2 \otimes \mathbf{I}_3, \end{aligned} \tag{45}$$

which can be invoked for correcting a single bit-flip ($\mathbf{X}$) error. The Hadamard gates, which carry out the unitary transformation we wish to protect, are arranged transversally, where the Hadamard gate is applied to each of the encoded logical qubits as seen in Fig. 7(a). Hence, the unitary transformation U_f can be expressed as

$$U_f = \mathbf{H}^{\otimes n}, \tag{46}$$

where the superscript $\otimes n$ of $\mathbf{H}$ represents the n-fold tensor product. The unitary transform U_f transforms the quantum state $|\overline{\psi_1}\rangle$ into quantum state $|\overline{\psi_2}\rangle$ as follows:

$$|\overline{\psi_2}\rangle = \alpha|++\rangle + \beta|--\rangle. \tag{47}$$

Based on Eq. (41), the stabilizer operators of Eq. (45) and the unitary transformation U_f of Eq. (46), we obtain the effective stabilizer generators $\widehat{S}_i$ for stabilizing the quantum state $|\overline{\psi_2}\rangle$ in Fig. 7(a) as follows:

$$\begin{aligned} \widehat{S}_1 &= \left(\mathbf{H}^{\otimes 3}\right)\left(\mathbf{Z}_1 \otimes \mathbf{I}_2 \otimes \mathbf{Z}_3\right)\left(\mathbf{H}^{\otimes 3}\right)^{\dagger} \\ &= (\mathbf{HZH}^{\dagger})_1 \otimes (\mathbf{HIH}^{\dagger})_2 \otimes (\mathbf{HZH}^{\dagger})_3 \\ &= \mathbf{X}_1 \otimes \mathbf{I}_2 \otimes \mathbf{X}_3, \end{aligned} \tag{48}$$

$$\begin{aligned} \widehat{S}_2 &= \left(\mathbf{H}^{\otimes 3}\right)\left(\mathbf{Z}_1 \otimes \mathbf{Z}_2 \otimes \mathbf{I}_3\right)\left(\mathbf{H}^{\otimes 3}\right)^{\dagger} \\ &= (\mathbf{HZH}^{\dagger})_1 \otimes (\mathbf{HZH}^{\dagger})_2 \otimes (\mathbf{HIH}^{\dagger})_3 \\ &= \mathbf{X}_1 \otimes \mathbf{X}_2 \otimes \mathbf{I}_3, \end{aligned} \tag{49}$$

which are capable of correcting a single phase-flip ($\mathbf{Z}$) error. Finally, to transform the physical qubits in the state of $|\overline{\psi_2}\rangle$ to the state of $U_f|\overline{\psi_0}\rangle$, we design the effective inverse encoder of $\widehat{\mathcal{V}}^{\dagger}$ based on Eq. (43) and we obtain the quantum circuit portrayed in Fig. 7(a). Therefore, the final state of $U_f|\overline{\psi_0}\rangle$ can be described as follows:

$$\begin{aligned} U_f|\overline{\psi_0}\rangle &= \mathbf{H}^{\otimes n}(|\psi\rangle \otimes |0\rangle^{\otimes(n-k)}) \\ &= \mathbf{H}^{\otimes k}|\psi\rangle \otimes (\mathbf{H}^{\otimes(n-k)} \otimes |0\rangle^{\otimes(n-k)}) \\ &= \mathbf{H}^{\otimes k}|\psi\rangle \otimes |+\rangle^{\otimes(n-k)}. \end{aligned} \tag{50}$$

The last term of $|+\rangle^{\otimes(n-k)}$ can be discarded during measurement, since it is no longer entangled. In this example, we arrive at $|++\rangle$. Finally, from the design example specified in Fig. 7(a), we acquire the desired output in the state of $\mathbf{H}^{\otimes k}|\psi\rangle = \mathbf{H}|\psi\rangle = \alpha|+\rangle + \beta|-\rangle$, given that we have $k = 1$ and $|\psi\rangle = \alpha|0\rangle + \beta|1\rangle$.

In this treatise, another technique of utilizing QSC for protecting the transversal quantum Clifford gates without the quantum encoder $\mathcal{V}$ is presented. In order to relax the assumption of having a perfect quantum encoder $\mathcal{V}$, all the $(n-k)$ auxiliarry qubits required for creating the encoded state of the physical qubits are initialized to the $|+\rangle$ state and then followed by stabilizer measurements as suggested in [62], [63]. The quantum circuit of tranversal Hadamard gates protected by a $1/3$-rate quantum repetition code is portrayed in Fig. 7(b). Let us denote the encoded state of physical qubits $\alpha|000\rangle + \beta|111\rangle$ of Eq. (44) as $|\overline{\psi_1}\rangle$ and the encoded state of physical qubits $\alpha|++\rangle + \beta|--\rangle$ of Eq. (47) as $|\overline{\psi_2}\rangle$. The quantum state $|\overline{\psi_0}\rangle$ of Fig. 7(b) can then be expressed as

$$|\overline{\psi_0}\rangle = (\alpha|0\rangle + \beta|1\rangle) \otimes |+\rangle \otimes |+\rangle. \tag{51}$$

Given that $|+\rangle = \frac{|0\rangle+|1\rangle}{\sqrt{2}}$, we can expand and rewrite the quantum state $|\overline{\psi_0}\rangle$ of Eq. (51) in terms of $|\overline{\psi_1}\rangle = \alpha|000\rangle + \beta|111\rangle$ as follows:

$$|\overline{\psi_0}\rangle = |\overline{\psi_1}\rangle + \mathbf{X}_2|\overline{\psi_1}\rangle + \mathbf{X}_3|\overline{\psi_1}\rangle + \mathbf{X}_2\mathbf{X}_3|\overline{\psi_1}\rangle, \tag{52}$$

where the notation of $\mathbf{X}_i$ indicates that Pauli matrix $\mathbf{X}$ is applied to the i-th qubit. The current quantum state of $|\overline{\psi_0}\rangle$ is in a form of superposition of $|\overline{\psi_1}\rangle$ states. More specifically, the action of stabilizer measurements ($S_i \in \mathcal{S}$) will result in collapsing the quantum state $|\overline{\psi_0}\rangle$ into one of the following possibilities: $|\overline{\psi_1}\rangle$, $\mathbf{X}_2|\overline{\psi_1}\rangle$, $\mathbf{X}_3|\overline{\psi_1}\rangle$, and $\mathbf{X}_2\mathbf{X}_3|\overline{\psi_2}\rangle$ with equal probabilities. The resultant collapsed quantum state $|\overline{\psi_1}\rangle$ is

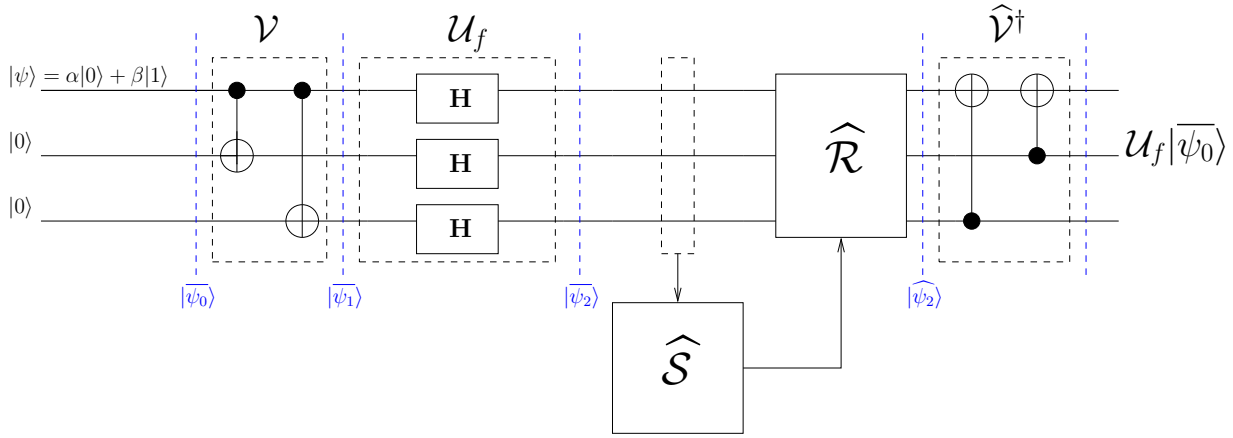

(a) Example of transversal implementation of Hadamard gates protected by a $1/3$-rate quantum repetition code with quantum encoder $\mathcal{V}$.

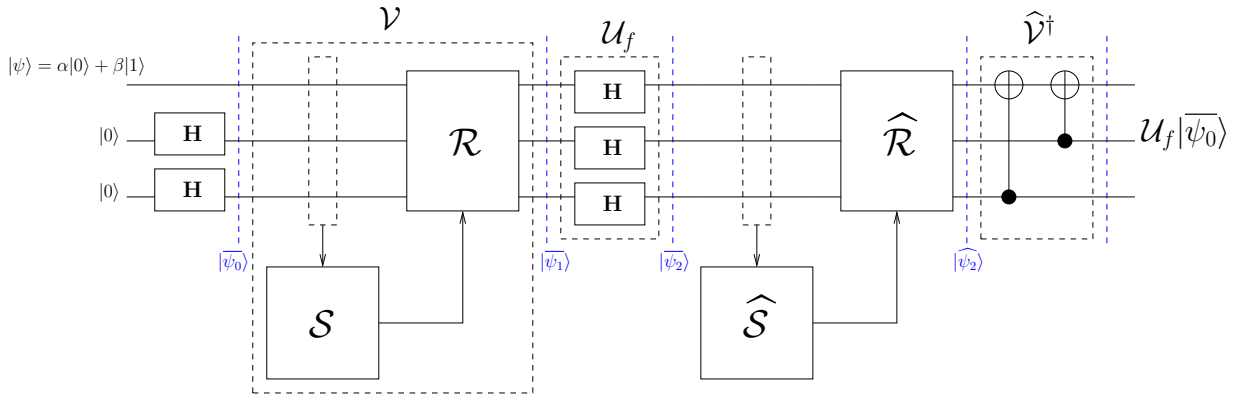

(b) Example of transversal implementation of Hadamard gates protected by a $1/3$-rate quantum repetition code with repeated stabilizer measurements.

Fig. 7: The realization of the transversal implementation of quantum gates protected by the $1/3$-rate quantum repetition code. The unitary operator U_f in these examples represents the transversal implementation of Hadamard gates.

determined by the ± 1 values gleaned from the stabilizer measurements $S_i \in \mathcal{S}$ of Fig. 7(b). Hence, the error recovery $\mathcal{R}$ is capable of transforming resultant collapsed quantum state back into the legitimate quantum state $|\overline{\psi_1}\rangle$. Hence, its action is similar to that of the scheme seen in Fig. 7(a) relying on the quantum encoder $\mathcal{V}$. Next, the action of the unitary operator U_f, which is represented by the transversal Hadamard gates of Eq. (46), transforms the quantum state $|\overline{\psi_1}\rangle$ into the quantum state $|\overline{\psi_2}\rangle$ as follows:

$$\begin{aligned} |\overline{\psi_2}\rangle &= U_f|\overline{\psi_1}\rangle \\ &= \alpha|++\rangle + \beta|--\rangle. \end{aligned} \tag{53}$$

From this point onwards, both the effective recovery operators $\widehat{\mathcal{R}}$ as well as the effective quantum inverse encoder $\widehat{\mathcal{V}}^\dagger$ of the schemes operating either with or without quantum encoder $\mathcal{V}$, are identical. Therefore, the error correction performance of the two schemes is also expected to be identical.

B. Transversal CNOT Gates

For our next example, we aim for conceiving the transversal implementation of CNOT gates protected by the $1/3$-rate quantum repetition code. The model is depicted in Fig. 8. For the scheme portrayed in Fig. 8(a), the initial state is defined by $|\psi\rangle = |\phi_1\rangle \otimes |\phi_2\rangle$ and our desired output is $\mathbf{CNOT}(|\phi_1\rangle \otimes |\phi_2\rangle)$, where $|\phi_1\rangle$ acts as the control qubit and $|\phi_2\rangle$ serves as the target qubit. The quantum encoder $\mathcal{V}$ of Fig. 8(a) encodes each of the logical qubits in the state of $|\phi_1\rangle$ and $|\phi_2\rangle$ independently, yielding the physical qubits in the state of $|\overline{\psi_1}\rangle = |\overline{\phi_1}\rangle \otimes |\overline{\phi_2}\rangle$, where $|\overline{\phi_1}\rangle$ and $|\overline{\phi_2}\rangle$ are the encoded logical qubits of $|\phi_1\rangle$ and $|\phi_2\rangle$, respectively. Therefore, the stabilizer operators S_i provided for the physical qubits in the state of $|\overline{\psi_1}\rangle$ in Fig. 8(a) are generated by the following stabilizer generators:

$$\begin{aligned} S_1 &= \mathbf{Z}_1 \otimes \mathbf{I}_2 \otimes \mathbf{Z}_3 \otimes \mathbf{I}_4 \otimes \mathbf{I}_5 \otimes \mathbf{I}_6, \\ S_2 &= \mathbf{Z}_1 \otimes \mathbf{Z}_2 \otimes \mathbf{I}_3 \otimes \mathbf{I}_4 \otimes \mathbf{I}_5 \otimes \mathbf{I}_6, \\ S_3 &= \mathbf{I}_1 \otimes \mathbf{I}_2 \otimes \mathbf{I}_3 \otimes \mathbf{Z}_4 \otimes \mathbf{I}_5 \otimes \mathbf{Z}_6, \\ S_4 &= \mathbf{I}_1 \otimes \mathbf{I}_2 \otimes \mathbf{I}_3 \otimes \mathbf{Z}_4 \otimes \mathbf{Z}_5 \otimes \mathbf{I}_6. \end{aligned} \tag{54}$$

In this example, the quantum gate that we try to protect is the CNOT gate. Therefore, the unitary transformation U_f of Fig. 8 represents the unitary matrix of the transversal CNOT gates. Now, let us denote the unitary matrix of the n transversal CNOT gates as $\overline{\mathbf{CNOT}}^n$. Therefore, the unitary transformation U_f of Fig. 8, can be expressed as a 64×64-element matrix

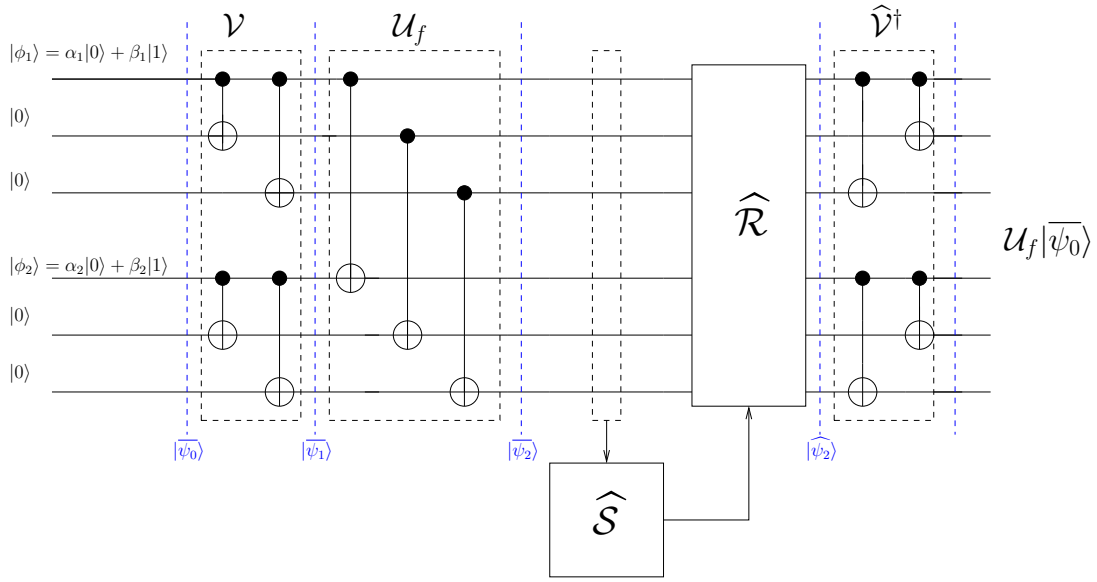

(a) Example of transversal implementation of CNOT gates protected by a $1/3$-rate quantum repetition code with quantum encoder $\mathcal{V}$.

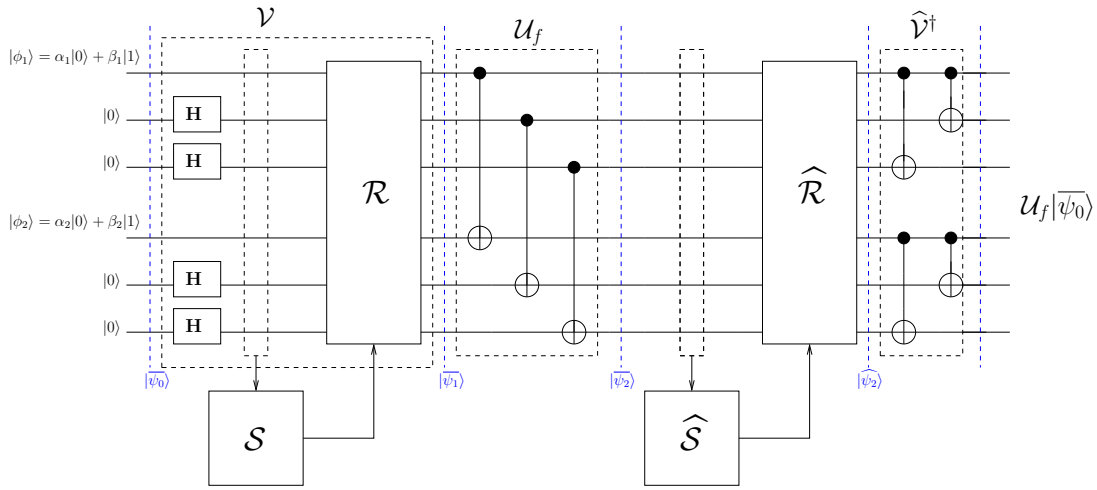

(b) Example of transversal implementation of CNOT gates protected by a $1/3$-rate quantum repetition code with repeated stabilizer measurements.

Fig. 8: The realization of the transversal implementation of CNOT gates protected by the $1/3$-rate quantum repetition code. The unitary operator U_f in these examples represents the transversal implementation of CNOT gates. The QSC-protected quantum gates can be realized with quantum encoder $\mathcal{V}$ or with repeated stabilizer measurements. Naturally, the scheme without quantum encoder $\mathcal{V}$ is favourable since it potentially eliminates the error propagation imposed by the CNOT gates.

by expanding the following transformation:

$$\begin{aligned} U_f &= \overline{\mathbf{CNOT}}^3 \\ &= |000\rangle\langle 000| \otimes \mathbf{I} \otimes \mathbf{I} \otimes \mathbf{I} + |001\rangle\langle 001| \otimes \mathbf{I} \otimes \mathbf{I} \otimes \mathbf{X} \\ &+ |010\rangle\langle 010| \otimes \mathbf{I} \otimes \mathbf{X} \otimes \mathbf{I} + |011\rangle\langle 011| \otimes \mathbf{I} \otimes \mathbf{X} \otimes \mathbf{X} \\ &+ |100\rangle\langle 100| \otimes \mathbf{X} \otimes \mathbf{I} \otimes \mathbf{I} + |101\rangle\langle 101| \otimes \mathbf{X} \otimes \mathbf{I} \otimes \mathbf{X} \\ &+ |110\rangle\langle 110| \otimes \mathbf{X} \otimes \mathbf{X} \otimes \mathbf{I} + |111\rangle\langle 111| \otimes \mathbf{X} \otimes \mathbf{X} \otimes \mathbf{X}. \end{aligned} \tag{55}$$

Based on the stabilizer generators S_i in Eq. (54) and the unitary transformation U_f of Eq. (55), we can obtain the effective stabilizer operators $\widehat{S}_i$ by applying Eq. (41), which formulated for protecting the state of $|\overline{\psi_2}\rangle$ in Fig. 8(a). Explicitly, the effective stabilizer operators $\widehat{S}_i$ is generated by the following stabilizer generators:

$$\begin{aligned} \widehat{S}_1 &= \mathbf{Z}_1 \otimes \mathbf{I}_2 \otimes \mathbf{Z}_3 \otimes \mathbf{I}_4 \otimes \mathbf{I}_5 \otimes \mathbf{I}_6, \\ \widehat{S}_2 &= \mathbf{Z}_1 \otimes \mathbf{Z}_2 \otimes \mathbf{I}_3 \otimes \mathbf{I}_4 \otimes \mathbf{I}_5 \otimes \mathbf{I}_6, \\ \widehat{S}_3 &= \mathbf{Z}_1 \otimes \mathbf{I}_2 \otimes \mathbf{Z}_3 \otimes \mathbf{Z}_4 \otimes \mathbf{I}_5 \otimes \mathbf{Z}_6, \\ \widehat{S}_4 &= \mathbf{Z}_1 \otimes \mathbf{Z}_2 \otimes \mathbf{I}_3 \otimes \mathbf{Z}_4 \otimes \mathbf{Z}_5 \otimes \mathbf{I}_6. \end{aligned} \tag{56}$$

Based on the commutativity property of stabilizer operators, where the multiplication among stabilizer operators will produce another valid stabilizer operator, we may rewrite the list of stabilizer generators given in Eq. (56). Hence, by multiplying $\widehat{S}_1$ and $\widehat{S}_3$ also by multiplying $\widehat{S}_2$ and $\widehat{S}_4$, we obtain the following effective stabilizer operators $\widehat{S}_i$ generated

by the following stabilizer generators:

$$\begin{aligned}\widehat{S}_1 &= \mathbf{Z}_1 \otimes \mathbf{I}_2 \otimes \mathbf{Z}_3 \otimes \mathbf{I}_4 \otimes \mathbf{I}_5 \otimes \mathbf{I}_6,\\ \widehat{S}_2 &= \mathbf{Z}_1 \otimes \mathbf{Z}_2 \otimes \mathbf{I}_3 \otimes \mathbf{I}_4 \otimes \mathbf{I}_5 \otimes \mathbf{I}_6,\\ \widehat{S}_3 &= \mathbf{I}_1 \otimes \mathbf{I}_2 \otimes \mathbf{I}_3 \otimes \mathbf{Z}_4 \otimes \mathbf{I}_5 \otimes \mathbf{Z}_6,\\ \widehat{S}_4 &= \mathbf{I}_1 \otimes \mathbf{I}_2 \otimes \mathbf{I}_3 \otimes \mathbf{Z}_4 \otimes \mathbf{Z}_5 \otimes \mathbf{I}_6. \end{aligned} \tag{57}$$

As we can observe, the resultant effective stabilizer operators $\widehat{S}_i \in \widehat{\mathcal{S}}$ of Eq. (57) are identical with the stabilizer operators $S_i \in \mathcal{S}$ of Eq. (54). Consequently, it demonstrates the convenience of exploiting the transversal implementation of CNOT gates. Since the effective stabilizer operators $\widehat{S}_i$ of Eq. (57) are identical to the stabilizer operators S_i of Eq. (54), the quantum circuit of the effective inverse encoder $\widehat{\mathcal{V}}^\dagger$ of Fig. 8 is also identical to the inverse encoder $\mathcal{V}^\dagger$ designed for transforming the state $|\overline{\psi_1}\rangle$ to the state $|\overline{\psi_0}\rangle$. Finally, the desired state for the output physical qubits based on the transversal configuration given in Fig. 8 can be formulated as

$$\begin{aligned} U_f|\overline{\psi_0}\rangle &= \overline{\mathbf{CNOT}}^n(|\phi_1\rangle \otimes |0\rangle^{\otimes(n-k)}, (|\phi_2\rangle \otimes |0\rangle^{\otimes(n-k)}))\\ &= \overline{\mathbf{CNOT}}^k(|\phi_1\rangle, |\phi_2\rangle) \otimes |00\rangle^{\otimes(n-k)}, \end{aligned} \tag{58}$$

where the last term represents the auxiliary qubits in the state of $|00\rangle^{\otimes(n-k)}$ that can be discarded after measurement, since they are no longer entangled with the logical qubits in the state of $\overline{\mathbf{CNOT}}^k(|\phi_1\rangle, |\phi_2\rangle)$. Given that we have $k = 1$ and $n = 3$ for our example in Fig. 8, we succesfully protect the unitary transformation of $\mathbf{CNOT}(|\phi_1\rangle, |\phi_2\rangle)$ at the end of our scheme. Therefore, we have outlined the general framework of QSC-protected transversal quantum gates.

Additionally, we also present the scheme of protecting transversal CNOT gates without the quantum encoder $\mathcal{V}$ in Fig. 8(b). Instead of using the quantum encoder $\mathcal{V}$ portrayed in Fig. 8(a), we can also utilize the scheme of Fig. 8(b), where the quantum encoder $\mathcal{V}$ is replaced with stabilizer masurements to create the legitimate encoded quantum state of the physical qubits. More specifically, the quantum state of the physical qubits $|\overline{\psi_1}\rangle$ of Fig. 8(a) is given by

$$\begin{aligned} |\overline{\psi_1}\rangle &= (\alpha_1|000\rangle + \beta_1\rangle|111\rangle) \otimes (\alpha_2|000\rangle + \beta_2\rangle|111\rangle)\\ &= \alpha_1\alpha_2|000\rangle|000\rangle + \alpha_1\beta_2|000\rangle|111\rangle\\ &+ \alpha_2\beta_1|111\rangle|000\rangle + \beta_1\beta_2|111\rangle|111\rangle. \end{aligned} \tag{59}$$

In Fig. 8(b), the physical qubits are prepared in the quantum state of $|\overline{\psi_0}\rangle$ as follows:

$$\begin{aligned} |\overline{\psi_0}\rangle &= (\alpha_1|0\rangle + \beta_1|1\rangle) \otimes |+\rangle \otimes |+\rangle\\ &\otimes (\alpha_2|0\rangle + \beta_2|1\rangle) \otimes |+\rangle \otimes |+\rangle. \end{aligned} \tag{60}$$

Given that $|+\rangle = \frac{|0\rangle+|1\rangle}{\sqrt{2}}$, we can expand and rewrite the quantum state $|\overline{\psi_0}\rangle$ of Eq. (60) in terms of $|\overline{\psi_1}\rangle$ of Eq. (59) as follows:

$$\begin{aligned} |\overline{\psi_0}\rangle &= |\overline{\psi_1}\rangle + \mathbf{X}_2|\overline{\psi_1}\rangle + \mathbf{X}_3|\overline{\psi_1}\rangle + \mathbf{X}_2\mathbf{X}_3|\overline{\psi_1}\rangle\\ &+ \mathbf{X}_5|\overline{\psi_1}\rangle + \mathbf{X}_2\mathbf{X}_5|\overline{\psi_1}\rangle + \mathbf{X}_3\mathbf{X}_5|\overline{\psi_1}\rangle + \mathbf{X}_2\mathbf{X}_3\mathbf{X}_5|\overline{\psi_1}\rangle\\ &+ \mathbf{X}_6|\overline{\psi_1}\rangle + \mathbf{X}_2\mathbf{X}_6|\overline{\psi_1}\rangle + \mathbf{X}_3\mathbf{X}_6|\overline{\psi_1}\rangle + \mathbf{X}_2\mathbf{X}_3\mathbf{X}_6|\overline{\psi_1}\rangle\\ &+ \mathbf{X}_5\mathbf{X}_6|\overline{\psi_1}\rangle + \mathbf{X}_2\mathbf{X}_5\mathbf{X}_6|\overline{\psi_1}\rangle + \mathbf{X}_3\mathbf{X}_5\mathbf{X}_6|\overline{\psi_1}\rangle\\ &+ \mathbf{X}_2\mathbf{X}_3\mathbf{X}_5\mathbf{X}_6|\overline{\psi_1}\rangle, \end{aligned} \tag{61}$$

where the notation of $\mathbf{X}_i$ indicates that Pauli matrix $\mathbf{X}$ is applied to the i-th qubit. Notice that the stabilizer operators of Eq. (54) are associated with 16 possible classical syndrome vectors, where each of the syndrome vectors is associated with one of the superimposed states given in Eq. (61). When the stabilizer measurements are performed, the superposition state of Eq. (61) will result in collapsing the quantum state $|\overline{\psi_0}\rangle$ into one of the following 16 possibilities: $|\overline{\psi_1}\rangle$, $\mathbf{X}_2|\overline{\psi_1}\rangle$, $\mathbf{X}_3|\overline{\psi_1}\rangle$, $\mathbf{X}_2\mathbf{X}_3|\overline{\psi_1}\rangle$, $\mathbf{X}_5|\overline{\psi_1}\rangle$, $\mathbf{X}_2\mathbf{X}_5|\overline{\psi_1}\rangle$, $\mathbf{X}_3\mathbf{X}_5|\overline{\psi_1}\rangle$, $\mathbf{X}_2\mathbf{X}_3\mathbf{X}_5|\overline{\psi_1}\rangle$, $\mathbf{X}_6|\overline{\psi_1}\rangle$, $\mathbf{X}_2\mathbf{X}_6|\overline{\psi_1}\rangle$, $\mathbf{X}_3\mathbf{X}_6|\overline{\psi_1}\rangle$, $\mathbf{X}_2\mathbf{X}_3\mathbf{X}_6|\overline{\psi_1}\rangle$, $\mathbf{X}_5\mathbf{X}_6|\overline{\psi_1}\rangle$, $\mathbf{X}_2\mathbf{X}_5\mathbf{X}_6|\overline{\psi_1}\rangle$, $\mathbf{X}_3\mathbf{X}_5\mathbf{X}_6|\overline{\psi_1}\rangle$, $\mathbf{X}_2\mathbf{X}_3\mathbf{X}_5\mathbf{X}_6|\overline{\psi_1}\rangle$, where the collapsed quantum state is determined by the classical syndrome vector obtained from stabilizer measurements. Therefore, we can apply the recovery operator $\mathcal{R}$ to obtain the encoded state of physical qubits of $|\overline{\psi_1}\rangle$ of Eq. (59). After the recovery operator is carried out, the unitary transformation U_f is applied to the quantum state $|\overline{\psi_1}\rangle$, which transforms the quantum state of $|\overline{\psi}_1\rangle$ into quantum state $|\overline{\psi}_1\rangle$ as follows:

$$|\overline{\psi_2}\rangle = U_f|\overline{\psi}_1\rangle. \tag{62}$$

Similar to transversal Hadamard gates, from this point onwards, all the effective stabilizer measurements, error recovery operators, and inverse encoder of both Fig. 8(a) and Fig. 8(b) are identical. Hence, we expect the error correction performance of the two schemes illustrated in Fig. 8 to be identical.

V. Error Model

In order to show the benefit of utilizing the framework exemplified in Section IV, we have to opt for a realistic quantum decoherence model of the system in order to produce the most realistic performance results. However, several assumptions have to be made in order to justify the proposed error model. Based on [75]–[78], we stipulate the idealized simplifying assumption that quantum decoherence may be imposed by single-qubit quantum gates, two-qubit quantum gates, as well as by the deleterious effects of the stabilizer measurements. In order to consider the decoherence inflicted by multiple components within our framework, we offer the following two propositions:

Proposition 1. An error-infested quantum encoder $\mathcal{V}$ and a unitary transformation U_f can be modeled as a perfect quantum encoder $\mathcal{V}$ and a perfect unitary transformation U_f followed by the quantum channel $P \in \mathcal{P}_n$. To elaborate a little further, the encoder of QSCs can be fully constructed from the quantum gates belonging to the Clifford group. Consequently, we can use the formulation of Eq. (29), which is illustrated in Fig. 4, in order to model the error propagation throughout the quantum encoder. More explicitly, let us provide an example using the quantum encoder of Steane's 7-qubit code, which

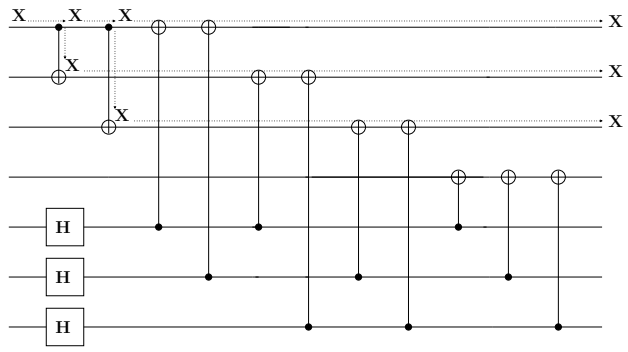

(a) The error propagation of a single bit-flip ($\mathbf{X}$) error at the input of first qubit.

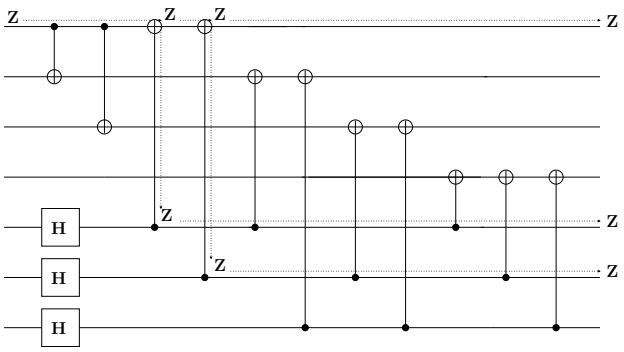

(b) The error propagation of a single phase-flip ($\mathbf{Z}$) error at the input of first qubit.

Fig. 9: The quantum encoder for Steane's 7-qubit code can be implemented purely consisting of quantum gates from the Clifford group. Therefore, a faulty quantum encoder of any QSC can be assumed to be modelled as a perfect quantum encoder followed by the quantum depolarizing channel. A single bit-flip ($\mathbf{X}$) error at the input can be transformed into three bit-flip errors at the output of quantum encoder $\mathcal{V}$ as shown in (a). Similarly, a phase-flip ($\mathbf{Z}$) inflicted at the input of quantum encoder $\mathbf{V}$ may propagate resulting three phase-flip error at the output as depicted in (b).

is equivalent to the quantum encoder of the distance-3 colour code, as portrayed in Fig. 9. We can observe from Fig. 9 that a single bit-flip ($\mathbf{X}$) error at the input of the quantum encoder is transformed into three separated bit-flip ($\mathbf{X}$) errors, which are accumulated at the output of the encoder $\mathcal{V}$. Similarly, a phase-flip ($\mathbf{Z}$) at the input of the quantum encoder propagating across the quantum encoder is transformed into three different phase-flip errors at three different locations at the output of the quantum encoder $\mathcal{V}$. Hence, in general, the severity of error propagation within the quantum encoder $\mathcal{V}$ is determined by the number of two-qubit quantum Clifford gates composing it.

Proposition 2. An error-infested stabilizer measurement of the QSC protecting the transversal quantum gates of Fig. 6(b) can be substituted by perfect stabilizer measurement and the quantum channel $P \in \mathcal{P}$ after the transversal configuration of quantum gates, which is illustrated in Fig. 10. This is also the natural consequences of the conjugation of Eq. (29). Since the $\mathbf{X}$ stabilizer operators anti-commute with the $\mathbf{Z}$ Pauli operator, only $\mathbf{Z}$-type errors are considered for $\mathbf{X}$ stabilizer measurements. Equivalently, since the $\mathbf{Z}$ stabilizer operators anti-commute with the $\mathbf{X}$ Pauli operator, only $\mathbf{X}$-type errors affect the result of $\mathbf{Z}$ stabilizer measurements.

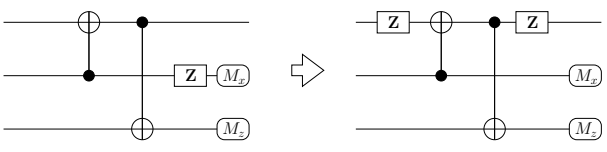

(a) Error on $\mathbf{X}$ stabilizer measurement.

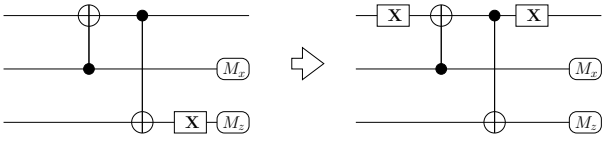

(b) Error on $\mathbf{Z}$ stabilizer measurement.

Fig. 10: An erroneous stabilizer measurement can be equivalently replaced by errors before and after the quantum circuit.

A. Source of Decoherence

By considering the potential sources of quantum-decoherence based on our proposed framework and also the nature of error propagation, we conclude that diverse sources of decoherence can be efficiently modelled as the accumulated quantum decoherence before and after the transversal quantum gates U_f, as explicitly shown in Fig. 11. To elaborate a little further, the quantum decoherence before the transversal quantum gates is constituted by $P_1 \in \mathcal{P}_n$ that corrupts the physical qubits in the state of $|\overline{\psi_1}\rangle$ by $\mathbf{X}$, $\mathbf{Z}$ and $\mathbf{Y}$-type errors independently with depolarizing probability of $p^{\mathbf{X}} = p^{\mathbf{Y}} = p^{\mathbf{Z}} = p_1/3$. Similarly, the quantum decoherence after the transversal gates is denoted by $P_2 \in \mathcal{P}_n$), which is described by the depolarizing probability of p_2, corrupting the physical qubits in the state of $|\overline{\psi_2}\rangle$.

It is important to note that each of the error operators P_1 and P_2 may encapsulate several sources of quantum decoherence. For example, observe from Fig. 11 that the error operator P_1 represents the decoherence from the quantum encoder $\mathcal{V}$ of Fig. 6(b), which is denoted by P_v. The error operator of $P_v \in \mathcal{P}_n$ is characterized by the depolarizing probability of p_v. The error operator of $P_2 \in \mathcal{P}_n$ encapsulates both the quantum decoherence imposed by the quantum gates P_u as well as the quantum decoherence imposed by the stabilizer measurement P_m. If the error operator P_u is specified by the depolarizing probability of p_u and the error operator P_m is specified by the depolarizing probability of p_m, the error operator P_2 can be determined by $P_m \cdot P_u = P_2 \in \mathcal{P}_n$.

Let us now consider the various error models available in the literature. Most of the error models used for evaluating the performance of QSCs designed for protecting quantum gates have three parameters, namely the error probability imposed by single-qubit quantum gates denoted by p_a, the error probability imposed by two-qubit quantum gates denoted by p_b, and the error probability imposed by the stabilizer measurements denoted by p_m. The *standard error model* of [76] assumes that $p_a = p_b = p_m = p$. By contrast, the *balanced error model*

of [76] assumes that the error rate imposed by the single-qubit quantum gates is $p_a = 4p/5$, as well as that by the two-qubit quantum gates is $p_b = p$, and finally that by the stabilizer measurements is given by $p_m = 8p/15$. From an experimental point of view, let us consider the *ion trap error model* of [76], where the parameters are defined by $p_1 = p/1000$, $p_2 = p$, and $p_m = p/100$. Since in this treatise we model the quantum decoherence imposed on each of the physical qubits as an individual and independent binary symmetric channel [9], [10], we have the model parameters of $p_a = p_m = p$ and $p_b \approx 2p$. A more detailed description of our error model used in our investigations will be provided in the following subsection.

The various error models characterize different technology platforms available for developing quantum computers. In this treatise, however, we focus our attention on performance of transversal quantum Clifford gates protected by two-dimensional QTECCs using classical simulations. Intuitively, we want the value of depolarizing probability to be as low as possible. However, state-of-the-art quantum gates have relatively low fidelity ranging between $90.00\% - 99.90\%$, for various technology platforms, such as spin electronics, photonics, superconducting, trapped-ion, and silicon implementations [14]–[22]. Fortunately, based on the threshold theorem [27], it is possible to construct a reliable quantum computer from unreliable quantum gates, given that the gate error probability is below a certain threshold value and that a sufficiently high overhead is allowed. Therefore, most of the studies on the QECCs aim for finding the specific gate error probability p_a, p_b, and p_m so that the QECCs do become capable of significantly improving the reliability of quantum computers.

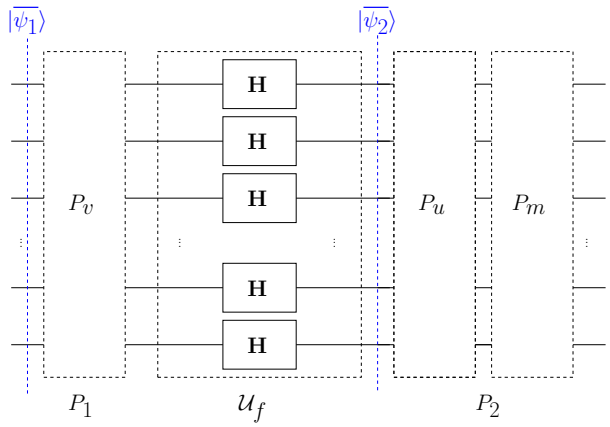

(a) Transversal Hadamard gates.

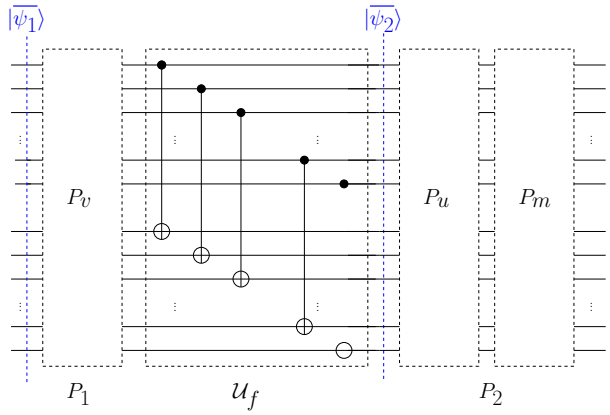

(b) Transversal CNOT gates.

Fig. 11: The potential quantum decoherence model imposed in our proposed system. There are several potential sources of quantum decoherences including the quantum encoder, quantum gates, and stabilizer measurement, denoted by P_v, P_u and P_m, respectively.

B. Faulty Quantum Gates

In this treatise, we rely on the model illustrated in Fig. 12, where each qubit experiences an independent quantum depolarizing channel characterized by its depolarizing probability. The metric used for evaluating the performance of our system is the qubit error rate (QBER) and the fidelity (F). The QBER is defined as the ratio between the number erroneous qubits to the total number of qubits. For a single-qubit quantum gate, which is exemplified by the Hadamard gate **H**, the QBER value can be represented as

$$\text{QBER}_{\text{Had}} = p, \tag{63}$$

where p is the depolarizing probability value of the single-qubit quantum decoherence caused by the imperfection of the quantum gate.

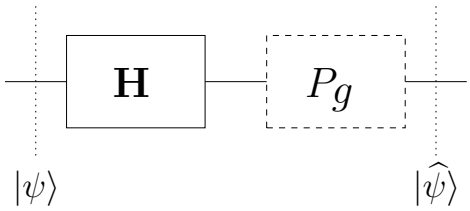

(a) The model of faulty Hadamard gate.

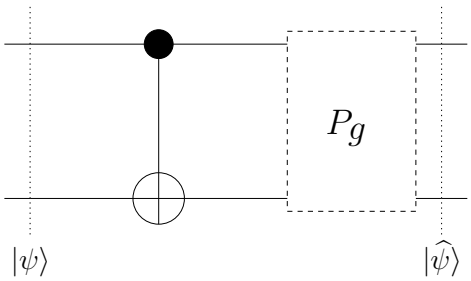

(b) The model of faulty CNOT gate.

Fig. 12: The unprotected faulty Hadamard and CNOT gates used as the benchmark. The Pauli channel $Pg \in \mathcal{P}$ is inflicted after the quantum gates.

The reliability of a quantum gate can also be quantified using its *fidelity*. Explicitly, the fidelity may be used to reflect the closeness of an ensemble of quantum states in the mixed-state to the desired pure state, which is formulated as follows [79]–[81]:

$$F = \langle\overline{\psi}|\rho|\overline{\psi}\rangle, \tag{64}$$

where $|\overline{\psi}\rangle$ is the desired pure state and ρ is the density matrix encapsulating the statistical characteristics of the mixed-states. The density matrix ρ is defined by

$$\rho = \sum_{i=1}^{N} p_i |\psi_i\rangle\langle\psi_i|, \tag{65}$$

where $|\psi_i\rangle$ represents all the possible quantum states in the ensemble and p_i is the probability of obtaining the quantum state $|\psi_i\rangle$, which is consequently constrained by the unity requirement of $\sum_{i=1}^{N} p_i = 1$. For a quantum Clifford gate, the relationship between fidelity and the QBER is as simple as

$$F = 1 - \text{QBER}, \tag{66}$$

where QBER is the qubit error ratio of the unprotected gate. Consequently, we obtain the analytical expression of the initial fidelity (F_{in}) for a Hadamard gate as a function of the depolarizing probability p as follows:

$$F_{\text{in}} = 1 - p. \tag{67}$$

Similar to the Hadamard gate, the fidelity of the CNOT gate can be defined using Eq. (66). Since a CNOT gate is a two-qubit quantum gate, the fidelity can be explicitly formulated as the probability of having the Pauli operator $\mathbf{I}$ on both the control qubit and the target qubit, which can be formulated as

$$\begin{aligned} F_{\text{in}} &= (1-p)(1-p) \\ &= 1 - 2p + p^2. \end{aligned} \tag{68}$$

Therefore, the QBER of a CNOT gate can be rewritten as follows:

$$\begin{aligned} \text{QBER}_{\text{CNOT}} &= 2p - p^2 \\ &\approx 2p, \end{aligned} \tag{69}$$

for $p \ll 1$. Therefore, given that p_a is the error rate or the QBER of a single-qubit quantum gate and p_b is the error rate or the QBER of a two-qubit quantum gate, we obtain the relationship between p_a and p_b obtained for classical simulation utilizing BSC as follows:

$$p_b \approx 2p_a. \tag{70}$$

Additionally, the relationship between the error rate of a single-qubit quantum gate p_a and the error rate of a stabilizer measurement p_m can be simply formulated as

$$p_m = p_a. \tag{71}$$

C. Effective Depolarizing Channel

As we have described in Subsection V-A, in the QSC-protected quantum transversal gates, there are multiple sources of decoherence. For example, in Fig. 11, the decoherence effects imposed by the transversal quantum gates and stabilizer measurements can be modelled by multiple subsequent quantum depolarizing channels. In order to simplify the analytical calculations and their approximation, we introduce the notion of *effective depolarizing channel*.

For example, let us assume that the first depolarizing channel is constituted by the error operator $P_1 \in \mathcal{P}_n$, which is characterized by the depolarizing probability $p_1 = p$, while the second depolarizing channel is constituted by the error operator $P_2 \in \mathcal{P}_n$, which is characterized by the depolarizing probability $p_2 = p$. Then, the probability of obtaining the Pauli matrix $\mathbf{I}$ at the output of two consecutive Pauli channels can be expressed as follows:

$$\begin{aligned} p_f^{\mathbf{I}} &= p_1^{\mathbf{I}} p_2^{\mathbf{I}} + p_1^{\mathbf{X}} p_2^{\mathbf{X}} + p_1^{\mathbf{Y}} p_2^{\mathbf{Y}} + p_1^{\mathbf{Z}} p_2^{\mathbf{Z}} \\ &= (1-p)(1-p) + \left(\frac{p}{3}\right)\left(\frac{p}{3}\right) + \left(\frac{p}{3}\right)\left(\frac{p}{3}\right) + \left(\frac{p}{3}\right)\left(\frac{p}{3}\right) \\ &= 1 - 2p + \frac{4}{3}p^2. \end{aligned} \tag{72}$$

Consequently, we obtain the following probability of experiencing the Pauli error $\mathbf{X}$, $\mathbf{Y}$, and $\mathbf{Z}$:

$$p_f^{\mathbf{X}} = p_f^{\mathbf{Y}} = p_f^{\mathbf{Z}} = \frac{2}{3}p - \frac{4}{9}p^2. \tag{73}$$

In other words, the effective depolarizing probability can be expressed as

$$\begin{aligned} p_f &= 2p - \frac{4}{3}p^2 \\ &\approx 2p. \end{aligned} \tag{74}$$

In can be concluded that a pair of depolarizing channels each characterized by the depolarizing probability p can be effectively viewed as a single quantum depolarizing channel associated with the aggregated depolarizing probability of $p_f = 2p$. Furthermore, the effective depolarizing probability p_f for c consecutive depolarizing channels, where each of the channels is characterized by an identical depolarizing probability p, can be approximated as

$$p_f \approx cp, \tag{75}$$

for $p \ll 1$.The expression given in Eq. (75) is our basis for deriving the analytical upper-bound expressions in Section VI.

We have to emphasize once again that this is one of the desirable properties of QTECCs compared to the rest of QSC family, namely that the number of stabilizer measurements applied to each physical qubit remains constant upon increasing the number of physical qubits n due to the convenient construction of the underlying lattice structure. As we can observe in Eq. (75), the effective depolarizing probability p_f is governed by the value of c and it is essentially the contribution from a number of stabilizer measurements experienced by each of the physical qubits. In case of the QTECCs, the value of c remains constant upon increasing the minimum distance d of the code and the number of the physical qubits n. For instance, the number of stabilizer measurements for colour codes is defined by the number of adjacent plaquettes for a given vertice. More specifically, each of the physical qubits in colour codes relies on at most six stabilizer measurements regardless of the specific minimum distance d of the code and of the number of physical qubits n. Similar findings are valid for surface codes. The number of stabilizer measurements relied upon by each of the physical qubits is defined by the number of vertices and plaquettes, given a particular edge of a

lattice. Each of the physical qubits in surface codes relies on at most four stabilizer measurements, regardless of the minimum distance d of the code and of the number of physical qubits n.

VI. Simulation Results and Performance Analysis

In order to evaluate the performance of the system considered, we exploited the classical-to-quantum Pauli isomorphism [9], [60]. To elaborate further, we generated two independent binary symmetric channels, where one of the channels modeled the bit-flip channel, while the other emulated the phase-flip channel. Since it is impossible to mimic identically the actual quantum depolarizing channel using two independent binary symmetric channels (BSCs), for approximating the quantum depolarizing channel having an equal probability of $\mathbf{X}$, $\mathbf{Z}$, and $\mathbf{Y}$-type of errors ($p^{\mathbf{X}} = p^{\mathbf{Z}} = p^{\mathbf{Y}} = p/3$), it is widely accepted that the flip probability of each BSCs in the classical simulation is adjusted to $p_{\mathbf{X}} = p_{\mathbf{Z}} = 2p/3$ [10], [11]. The maximum-likelihood hard-decision decoding technique was invoked, which was translated into a look-up table (LUT) based decoder. For the full exposure of how we conceived the LUT decoder, we refer the reader to [60]. We take the value of frame error rate (FER) from the classical simulation to potray the QBER, since we concern with unitary transformation on the arbitrary and unknown quantum state.

A. Simple Examples

In this section, we present the simplest scenario of transversal Hadamard gates and CNOT gates protected by quantum repetition codes. Let us revisit Fig. 7 and observe the associated QBER performance. Based on the error model described in Section V, the quantum depolarizing channel $P_g \in \mathcal{P}_n$ associated with the depolarizing probability p corrupted the quantum state of the physical qubits $|\overline{\psi_2}\rangle$. For the simplest scenario here, we assumed that the quantum encoder $\mathcal{V}$ and the syndrome measurement were also error-free.

For the transversal Hadamard gates protected by a $1/3$-rate quantum repetition code, which is illustrated in Fig. 7, the simulation results are portrayed in Fig. 13. We also have included the performance results for transversal Hadamard gates protected by $1/5$-rate and $1/7$-rate quantum repetition codes. Naturally, the quantum repetition codes can only protect the transversal Hadamard gates from one type of error, either the phase-flip or the bit-flip errors. In other words, they are not capable of protecting the quantum gates from a more realistic quantum depolarizing channel. Furthermore, reducing the quantum coding rate - for quantum repetition codes this only allows increasing the error correction capability for either bit-flip or phase-flip errors - imposes increased quantum decoherence on our system, which is shown explicitly by the increase of QBER in Fig. 13. To elaborate further, upon increasing the number of qubits, we only increase the error correction capability for either phase-flip or bit-flip errors. Consequently, the deleterious effect of other types of errors imposed by the quantum depolarizing channel is accumulated and left uncorrected.

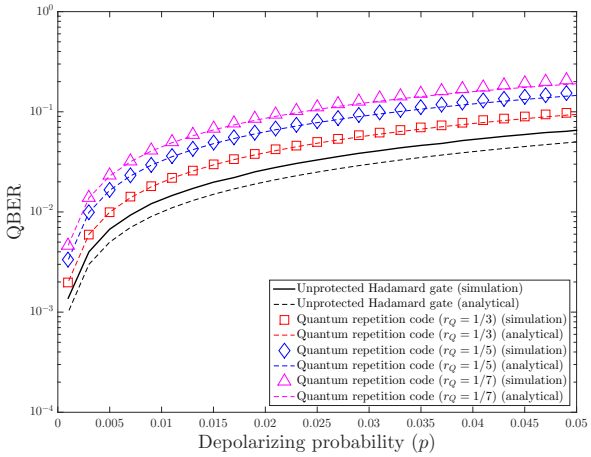

Fig. 13: QBER performance of the transversal Hadamard gates protected by $1/3$, $1/5$, and $1/7$-rate quantum repetition codes. We applied the depolarizing channel after the transversal configuration of Hadamard gates, where the depolarizing channel is characterized by the depolarizing probability p.

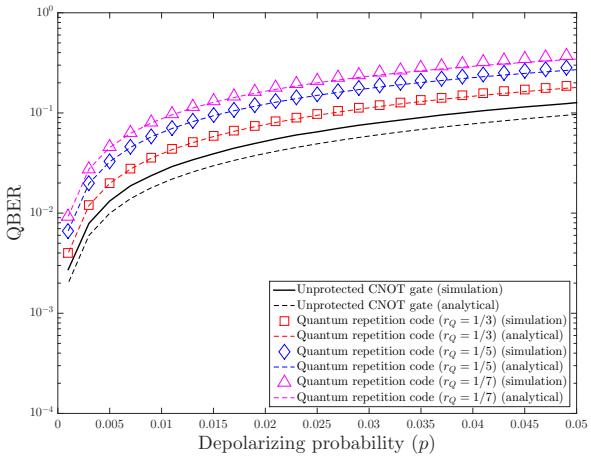

Fig. 14: QBER performance of transversal CNOT gates protected by $1/3$, $1/5$, and $1/7$-rate quantum repetition codes. We applied the depolarizing channel after the transversal configuration of CNOT gates, where the depolarizing channel is characterized by the depolarizing probability p.

We have also invoked our QSC-protected scheme for transversal two-qubit Clifford quantum gates, as exemplified by the CNOT gate. We portray the performance of an unprotected CNOT gate along with that of its QSC-protected counterpart utilizing a $1/3$-rate quantum repetition code, as illustrated in Fig. 8, in Fig. 14. Furthermore, we also have included the QBER performance curves of $1/5$-rate and $1/7$-rate quantum repetition codes. As expected, similar to transversal Hadamard gates, instead of being improved, the QBER performance of transversal CNOT gates is degraded upon reducing the quantum coding rate. Again, invoking QSCs for protecting quantum gates remains futile if we only consider protecting one type of errors. In conclusion, we have to employ

QSCs, which are capable of correcting the bit-flip, phase-flip as well as the simultaneous bit-flip and phase-flip errors.

B. QTECC-Protected Transversal Hadamard Gates

In this section, we utilized the more practical QTECCs as the subtitutes for the above-mentioned quantum repetition codes, since the QTECCs are capable of mitigating both bit-flip and phase-flip errors. More specifically, we considered colour codes [34], rotated-surface codes [35], and surface codes [33], exhibiting a minimum distance of $d = 3$ in our model of Fig. 6(b). For this scenario, we used the assumption that the encoded physical qubits can be created fault-tolerantly, hence the quantum encoder $\mathcal{V}$ was assumed to be error-free, or we can utilize the scheme without the quantum encoder $\mathcal{V}$ as we have described earlier in Section IV. The quantum depolarizing channel was inflicted by the quantum unitary operation U_f and also by the stabilizer measurements. The error operator $P_u \in \mathcal{P}_n$ imposed by the unitary operation U_f was characterized by the depolarizing probability $p_u = p$. However, for the stabilizer measurements, as we have mentioned in Section II, each of the physical qubits will have a constant number of measurement for each $\mathbf{X}$ and $\mathbf{Z}$ stabilizer operators. More explicitly, for surface codes and rotated-surface codes, each of the physical qubits will have at most two interactions for each $\mathbf{X}$ and $\mathbf{Z}$ stabilizer measurements, while for colour codes each of the physical qubits will have at most three interactions for each $\mathbf{X}$ and $\mathbf{Z}$ stabilizer measurements.

To elaborate a litlle further, due to the stabilizer measurements, we encountered four additional consecutive depolarizing channels after the error operator P_u imposed by the unitary operation U_f for surface and rotated-surface codes. Therefore, we had five consecutive depolarizing channels, where each of the error operators $P_i \in \mathcal{P}_n$ for $i = \{1, 2, 3, 4, 5\}$ was characterized by the depolarizing probability $p_i = p$. Similarly, for colour codes we inflicted six additional consecutive depolarizing channels after the error operator P_u imposed by the unitary operation U_f, hence we imposed seven consecutive depolarizing channels after unitary operation U_f, where each of the error operators $P_i \in \mathcal{P}_n$ for $i = \{1, 2, 3, 4, 5, 6, 7\}$ was also characterized by depolarizing probability $p_i = p$.

Formally, the effective error operator P_f after c consecutive error operators P_i can be expressed as

$$P_f = \prod_{i=1}^{c} P_i \text{ for } P_i \in \mathcal{P}_n. \tag{76}$$

For c consecutive depolarizing channels, the j-th qubit from n physical qubits will experience independently the effective error operators P_f, which is defined as

$$P_{f,j} = \prod_{i=1}^{c} P_i, \text{ for } \forall P_i \in \mathcal{P}_1^*. \tag{77}$$

Since there are c consecutive depolarizing channels, the probability of obtaining identity matrix $\mathbf{I}$ is equal to the sum of all probabilities from all the possible combinations of $P_{f,j}$ resulting in Pauli matrix $\mathbf{I}$, where we assume that $p^{\mathbf{I}} = (1-p)$ and $p^{\mathbf{X}} = p^{\mathbf{Y}} = p^{\mathbf{Z}} = p/3$. Therefore, the effective probability

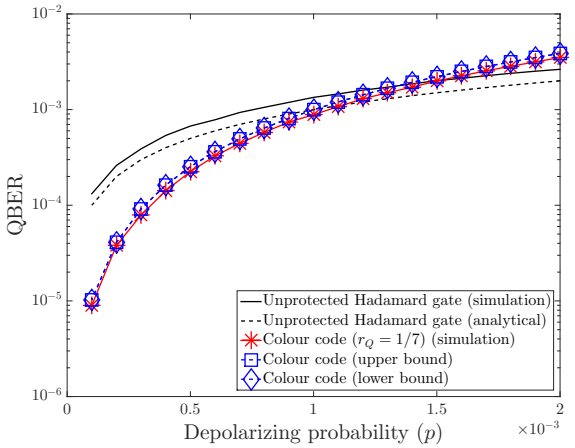

(a) Colour code.

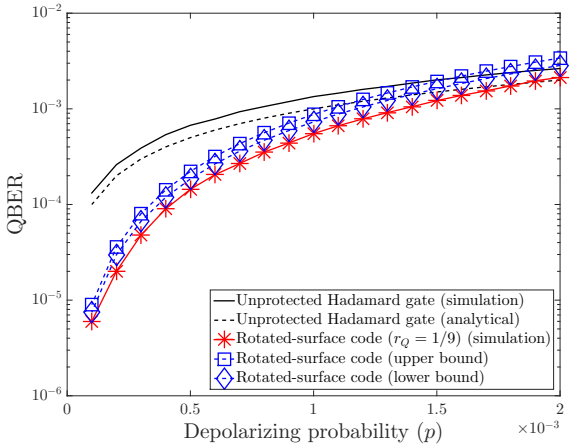

(b) Rotated-surface code.

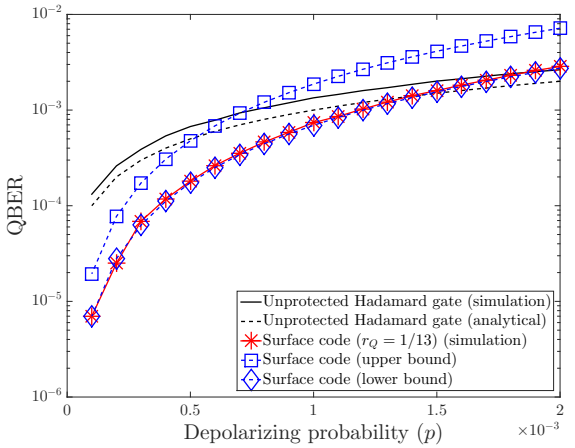

(c) Surface code.

Fig. 15: QBER performance for transversal Hadamard gates protected by distance-3 QTECCs over quantum depolarizing channel. The quantum decoherence is inflicted after the transversal configuration of Hadamard gates, where the error operators of $\prod_{i=1}^{c} P_i \in \mathcal{P}_n$ are defined by $p_i = p$. The number of consecutive error operators $c = 7$ for colour codes and $c = 5$ for surface and rotated-surface codes.

$$p_f^{\mathbf{I}} = (1-p)^5 + 30(1-p)^3\left(\frac{p}{3}\right)^2 + 60(1-p)^2\left(\frac{p}{3}\right)^3 + 105(1-p)\left(\frac{p}{3}\right)^4 + 60\left(\frac{p}{3}\right)^5$$
$$= 1 - 5p + \frac{40}{3}p^2 - \frac{160}{9}p^3 + \frac{320}{27}p^4 - \frac{256}{81}p^5. \quad (74)$$

$$p_f = 1 - p_f^{\mathbf{I}}$$
$$= 5p - \frac{40}{3}p^2 + \frac{160}{9}p^3 - \frac{320}{27}p^4 + \frac{256}{81}p^5. \quad (75)$$

of obtaining Pauli matrix $\mathbf{I}$ for five consecutive depolarizing channels can be expressed as shown in Eq. (74).

To elaborate a little further, we can infer from Eq. (74) that there are 30 possible combinations from $\prod_{i=1}^{5} P_i$ which give us $P_{f,j} = \mathbf{I}$ consisting of two non-identity Pauli operators $P_i \in \mathcal{P}_1^*$, 60 combinations consisting of three non-identity Pauli operators, 105 combinations consisting of four non-identity Pauli operators, and finally, 60 combinations consisting of five non-identity Pauli operators. Therefore, the effective depolarizing probability p_f for $c = 5$ can be formulated as shown in Eq. (75). However, in case of $p \ll 1$, the effective depolarizing probability can be approximated as

$$p_f \approx 5p, \quad (76)$$

as we have suggested earlier in Eq. (75).

Similarly, for $c = 7$, the sum of the probabilties from all of the possible combinations $P_{f,j}$ resulting in the Pauli matrix $\mathbf{I}$ can be expressed as shown in Eq. (77). Therefore, the effective depolarizing probability p_f for $c = 7$ can be expressed as portrayed in Eq. (78). Again, for $p \ll 1$, the value of p_f in Eq. (78) can be approximated as

$$p_f \approx 7p, \quad (79)$$

as we have suggested in Eq. (75).

We have simulated the system using the quantum-to-classical Pauli isomorphism for simulating the QSCs. The simulation results are portrayed in Fig. 15. The performance of the proposed scheme is quantified using the QBER versus the depolarizing probability p. For a minimum distance of $d = 3$, based on the code parameters given in Table II, the quantum coding rate r_Q of colour codes, of rotated-surface codes, as well as of surface codes are $1/7$, $1/9$, and $1/13$, respectively. In Fig. 15, we can observe the QBER performance improvement upon applying the scheme given in Fig. 6(b) compared to the unprotected quantum gates, especially for depolarizing probabilitiy values of $p < 2\times10^{-3}$.

In general, the analytical QBER performance of QSC-protected single-qubit quantum gates can be calculated as follows:

$$\text{QBER}^{(1)}_{\text{approx}}(n,d,p) = 1 - \sum_{i=0}^{n} A_i \binom{n}{i} p^i (1-p)^{n-i}, \quad (80)$$

where A_i is a real number coefficient portraying the success probability of correcting the error patterns having weight i. For a large number of n, finding the value of A_i for each of i becomes an intractable problem. One example of works of finding these A_i values specifically for colour codes can be seen in [82], where the authors successfully characterized the A_i values for colour codes up to minimum distance of $d = 7$. However, for non-degenerate QSCs, the analytical QBER performance can be approximated using the following upper-bound as described in [38], [60] denoted by $\text{QBER}^{(1)}_{\text{upper}}$ as follows:

$$\text{QBER}^{(1)}_{\text{upper}}(n,d,p) = 1 - \sum_{i=0}^{t=\lfloor \frac{d-1}{2} \rfloor} \binom{n}{i} p^i (1-p)^{n-i}$$
$$= \sum_{i=t+1}^{n} \binom{n}{i} p^i (1-p)^{n-i}, \quad (81)$$

where for QSCs-protected transversal single-qubit gates $p = p_f$, which in our case is the effective depolarizing probability defined by Eq. (75) for rotated-surface and surface codes and by Eq. (78) for colour codes.

To elaborate a little further, the upper-bound of Eq. (81) characterizes the worst-case performance assuming that any syndrome associated with an error pattern beyond the error correction capability of the quantum code is ignored, because attempting to correct these errors may potentially introduce additional errors. However, this decoding method does not exploit the full benefit of all the syndromes. For instance, for a distance-3 surface code, we have $n = 13$ and $k = 1$. Hence, we have $|\mathcal{G}| = n - k = 12$. Since the surface codes belong to the family of CSS-type QSCs, the syndrome operator $G_i \in \mathcal{G}$ is invoked for correcting the bit-flip and phase-flip errors separately. Consequently, for a distance-3 surface code, we have six stabilizer operators dedicated to the correction of bit-flip errors ($|\mathcal{G}_z| = 6$) and six stabilizer operators dedicated to the correction of phase-flip errors ($|\mathcal{G}_x| = 6$). Since each of the syndrome measurement values is associated with an element of the syndrome vector $\mathbf{s}$, we have a total of 64 possible syndrome vectors $\mathbf{s}$. From Eq. (27), we know that a distance-3 surface code is capable of correcting a single qubit error caused by a both bit-flip, a phase flip, or both. Consequently, from the total of 64 possible syndrome vectors $\mathbf{s}$, only 14 syndrome vectors are actually associated with recoverable error patterns. More explicitly, the all-zero syndrome vector is associated with an error-free quantum state of the physical qubits and 13 syndrome vectors are associated with single bit-flip or phase-flip error patterns. The remaining 50 syndromes are capable of detecting error patterns exhibiting an error weight beyond the error correction capability of the distance-3 surface code, although the decoder cannot make a definitive error recovery decision from these remaining syndromes. This is because each of them may be associated with multiple error patterns exhibiting an the identical error weight. Therefore, in the upper-bound formulation of Eq. (81), these remaining

$$p_f^{\mathbf{I}} = (1-p)^7 + 63(1-p)^5\left(\frac{p}{3}\right)^2 + 210(1-p)^4\left(\frac{p}{3}\right)^3 + 735(1-p)^3\left(\frac{p}{3}\right)^4 + 1260(1-p)^2\left(\frac{p}{3}\right)^5 + 966(1-p)\left(\frac{p}{3}\right)^6 + 756\left(\frac{p}{3}\right)^7$$
$$= 1 - 7p + 28p^2 - \frac{560}{9}p^3 + \frac{2270}{27}p^4 - \frac{1792}{27}p^5 + \frac{5488}{243}p^6 - \frac{3711}{729}p^7. \quad (77)$$

$$p_f = 1 - p_f^{\mathbf{I}}$$
$$= 7p - 28p^2 + \frac{560}{9}p^3 - \frac{2270}{27}p^4 + \frac{1792}{27}p^5 - \frac{5488}{243}p^6 + \frac{3711}{729}p^7. \quad (78)$$

TABLE II: The code parameters for various QTECCs based on the minimum distance d of the code [38].

Codes type	**Dimension**	**Number of physical qubits** (n)	**Number of stabilizers** $(\lvert\mathcal{S}\rvert)$	**Number of logical qubits** (k)
Colour [34]	d^*	$\frac{1}{4}\left(3d^2+1\right)$	$\frac{1}{4}\left(3d^2-3\right)$	1
Rotated-surface [35]	$d\times d$	d^2	d^2-1	1
Surface [33]	$d\times d$	$2d^2-2d+1$	$2d^2-2d$	1
Toric [32]	$d\times d$	$2d^2$	$2d^2-2$	2

* for triangular colour codes the dimension is defined by the side length of the equilateral triangle

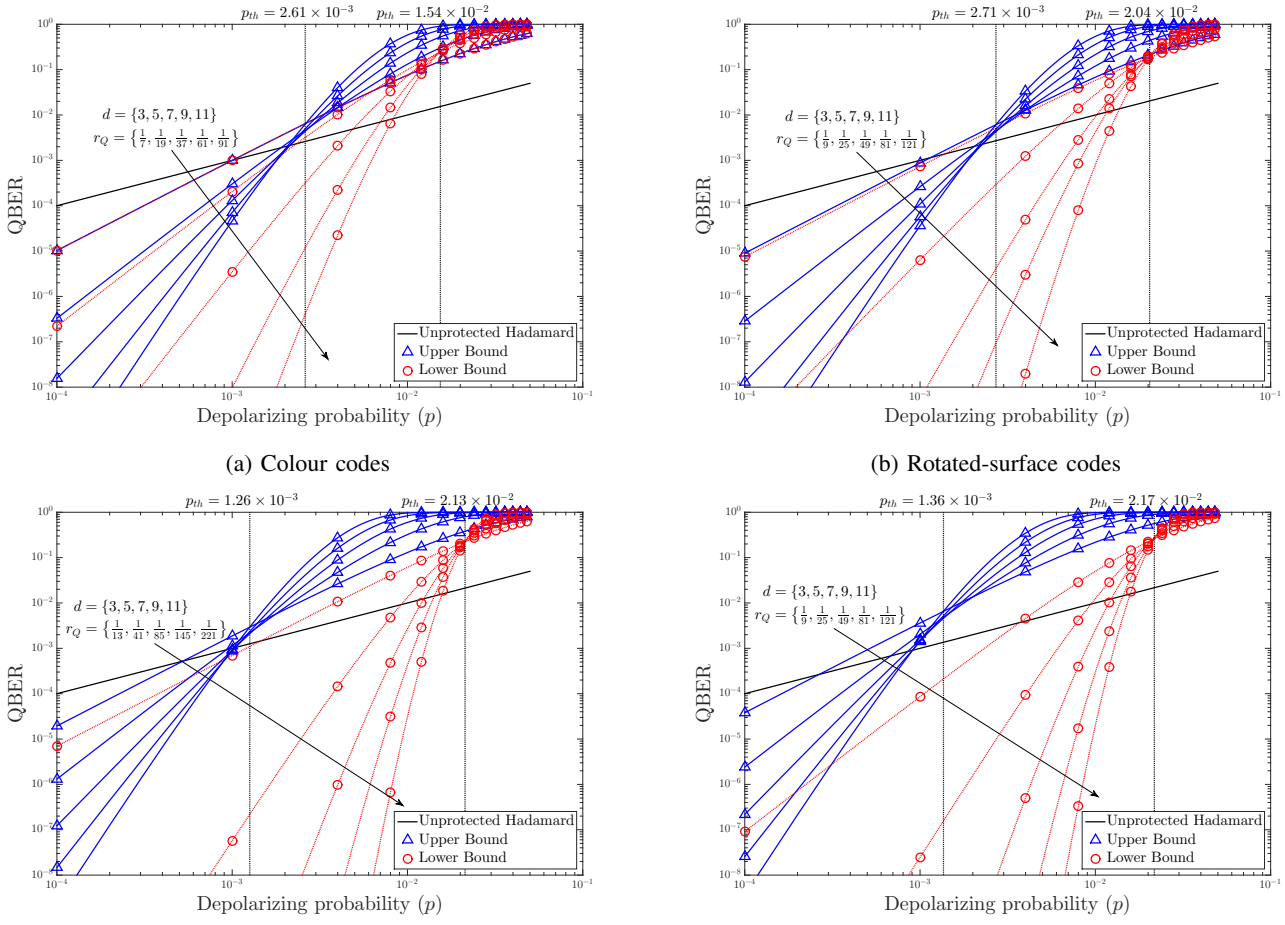

(a) Colour codes

(b) Rotated-surface codes

(c) Surface codes

(d) Toric codes

Fig. 16: Upper-bound and lower-bound analytical QBER performance curves of the transversal implementation of Hadamard gates protected by QTECCs.

50 syndrome vectors are ignored, because making a wrong decision, for instance by making a random decision for the error recovery operator, will further degrade the quantum state of the physical qubits instead of improving it.

In order to provide a confidence interval for the QBER performance of the QSCs for protecting single-qubit quantum gates, we characterize the lower-bound performances of the CSS-type QSCs based on the classical sphere-packing

bound [83], [84], which is also known as the quantum Gilbert-Varshamov (GV) bound [5], [60]. Formally, the lower-bound of the analytical QBER performance can be defined as follows [83], [84]:

$$\text{QBER}^{(1)}_{\text{lower}}(n,d,p) = 1 - \sum_{i=0}^{t'+1} A(i) p^i (1-p)^{n-i}, \tag{82}$$

where for the QSCs-protected tranversal single-qubit gates we have $p = pf$ and $A(i)$ is a positive integer obeying

$$\sum_{i=0}^{t'+1} A_i \leq 2^{(n-k)/2}, \text{ where } A_i = \binom{n}{i}. \tag{83}$$

Consequently, the final coefficient $A_{t'+1}$ is given by

$$A_{t'+1} = 2^{(n-k)/2} - \sum_{i=0}^{t'} A_i. \tag{84}$$

If the final coefficient is $A_{t'+1} = 0$, the code construction is referred to as a perfect CSS-type QSC. Otherwhise, the code is referred to as a quasi-perfect CSS-type QSC.

For instance, based on Eq. (81), the upper-bound of analytical QBER performance of a distance-3 surface code can be approximated as

$$\text{QBER}^{(1)}_{\text{upper}}(13,3,p_f) = 1 - (1-p_f)^{13} - 13 p_f (1-p_f)^{12}. \tag{85}$$

By comparison, based on Eq. (82), the lower-bound of analytical QBER performance of a distance-3 surface code can be approximated as

$$\text{QBER}^{(1)}_{\text{lower}}(13,3,p_f) = 1 - (1-p_f)^{13} - 13p(1-p_f)^{12} - 50 p_f^2 (1-p_f)^{11}. \tag{86}$$

The analytical upper-bound QBER performance of Eq. (81) and the lower-bound of Eq. (82), as well as the simulation results for the transversal Hadamard gates protected by selected distance-3 QTECCs are depicted in Fig. 15. In Fig. 15(a), we observe that the upper-bound analytical QBER performance of Eq. (81) is a very good approximation for the QBER performance from the simulation results. It is due to the fact that the construction of distance-3 colour code is identical with the 7-qubit Steane's code, which is a non-degenerate QSC. In general, Eq. (81) is a good approximation for non-degenerate QSCs. By contrast, a slightly different phenomenon can be obseved in Fig. 15(b) and 15(c), where the simulation results are closer with the lower-bound analytical QBER performance owing to their highly degenerate property.

Next, in Fig. 16, we portray the analytical upper-bound and the lower-bound QBER performance of transversal Hadamard gates protected by QTECCs for various minimum distance values. More specifically, we calculate the upper-bound QBER performance of colour codes, rotated-surface codes, surface codes, and toric codes having the minimum distances of $d = \{3,5,7,9,11\}$ using Eq. (81) and their lower-bound QBER performances using Eq. (82). The code parameters of the QTECCs used for calculating the upper-bound and lower-bound QBER performance are summarized in Table II. One of the unique properties of QTECCs is that upon increasing the minimum distance of the code d, we simultaneously increase the number of the pysical qubits length n and decrease the quantum coding rate r_Q [38]. The quantum coding rate r_Q portrayed in Fig. 16 is calculated using Eq. (26), where the number of logical qubits k and the number of physical qubits n are also given in Table II.

Increasing the error correction capability of QTECCs means that we simultaneously increase the number of auxiliary qubits and reduce the quantum coding rate r_Q. On the other hand, at high error rates, even powerful QECCs having a lower quantum coding rate often carry out flawed corrections, hence actually degrading the QBER more at high depolarizing probability values than their higher-rate counterparts. The superior error correction capability of the lower rate quantum codes start to impose below a specific depolarizing probability p, which we refer to as the *depolarizing probability threshold* (p_{th}). More specifically, p_{th} represents the point below which increasing the error correction capability of a quantum code is considered to be beneficial. Additionally, the value of p_{th} also can be used to infer the asymptotic performance of the QTECCs exhibiting a large number of physical qubits, where the quantum coding rate r_Q aprroches zero. In Fig. 16, the p_{th} is denoted by a dashed line at the cross-over point of the QBER performance curves. First, we obtain the upper-bound of p_{th} for colour codes, rotated-surface codes, surface codes, and toric codes as follows: 2.61×10^{-3}, 2.71×10^{-3}, 1.26×10^{-3}, and 1.36×10^{-3}, respectively. These specific p_{th} values are obtained by taking into account the errorneous stabilizer measurements. Specifically, each of the physical qubits of rotated-surface and surface codes experience only at most two $\mathbf{X}$ and two $\mathbf{Z}$ stabilizer measurements, while for colour codes, each of the physical qubits experience at most only three $\mathbf{X}$ and three $\mathbf{Z}$ stabilizer measurements. These numbers of the stabilizer measurements experienced by each of the physical qubits are independent to the total number of the physical qubits. In a case where we want to consider that we have perfect stabilizer measurements, indeed we can achieve a higher p_{th} values. We can simply use Eq. (75) and (78) to obtain the p_{th} values associated with error-free stabilizer measurements. More specifically, we obtain the p_{th} values as follows: 1.83×10^{-2}, 1.36×10^{-2}, 6.30×10^{-3}, and 6.80×10^{-3}, respectively, for colour, rotated-surface, surface, and toric codes.

Secondly, in Fig. 16, we can also observe the lower-bound of the p_{th} values given by: 1.54×10^{-2}, 2.04×10^{-2}, 2.13×10^{-2}, and 2.17×10^{-2}, respectively, for colour, rotated-surface, surface, and toric codes, which are associated with errorneous stabilizer measurements. Similarly, when we assume that we have error-free stabilizer measurements, the p_{th} values obtained are: 10.78%, 10.20%, 10.65%, and 10.85%, respectively, for colour, rotated-surface, surface, and toric codes. We observe that all the p_{th} lower bound values are in the proximity of $p_{th} \approx 11\%$, which is close to the quantum hashing bound for dual-containing CSS-type QSCs, formulated as:

$$C_Q = 1 - 2H(p), \tag{87}$$

where $H(p)$ is the binary entropy of p defined by $H(p) =$

$-p\log_2 p-(1-p)\log_2(1-p)$. Since the quantum coding rate of two-dimensional QTECCs tends to zero ($r_Q \to 0$) for a large n ($n \to \infty$), we find that in the asymptotical limit, the QBER performance of QTECCs approaches the ultimate hashing limit of dual-containing CSS-type QSCs, which is given by $p^* = 11\%$, as we have $r_Q = 0$. It is important to note that the quantum GV bound is relaxed optimistic lower-bound for non-degenerate QSCs. We also have to mention that the value $p^* = 11\%$ is also obtained in a different way in [82].

Finally, we present the performance of the transversal single-qubit quantum ggates protected by QSCs in terms of the fidelity (F_{th}) of each of the single-qubit quantum gate. Based on Eq. (64), we define the output fidelity as follows:

$$F_{\text{out}} = 1 - \text{QBER}_{\text{protected}}. \tag{88}$$

Since for asymptotical limit the QBER performance approaches the p_{th} value, we can also determine the fidelity threshold (F_{th}), which is defined as the minimum fidelity required for each of the quantum gates in order to benefit from employing the transversal quantum gates protected by the QSCs. Explicitly, the value of F_{th} for a single-qubit quantum gate can be simply determined as follows:

$$F_{\text{th}} = 1 - p_{th}. \tag{89}$$

Based on all the results presented in Fig. 16, we can obtain the upper-bound of the F_{th} for single-qubit quantum Clifford gates as follows: 99.74%, 99.73%, 99.87%, and 99.86%, respectively, for colour codes, rotated-surface codes, surface codes, and toric codes. Similarly, we also obtain the lower-bound of the F_{th} for single-qubit quantum Clifford gates from Fig. 16 as follows: 98.48%, 97.96%, 97.87%, and 97.83%, respectively, for colour codes, rotated-surface codes, surface codes, and toric codes. These F_{th} values mark the minimum requirement for the physical implementation of the single-qubit quantum gates if the implementation of QECCs within the quantum computers is considered. We have demonstrated that any quantum gates exhibiting lower F_{th} values will not provide any benefit of reliability improvement offered by the QECCs. Finally, all the results presented in this subsection are summarized in Table III.

C. QTECC-Protected Transversal CNOT Gates

Following similar investigations to those in Subsection VI-B, we also employed the family of QTECCs for protecting the transversal CNOT gates. For the transversal configuration of CNOT gates, we have two sets of QSCs, one QSC is invoked for protecting the physical control qubits and another one is for the physical target qubits. We assumed the QSCs used for both target and control qubits are identical. Due to the stabilizer preservation of QSCs after the transversal CNOT gates, as demonstrated in Section IV, each of the QSCs handles the errors inherent in the target qubits and in the control qubits independently. The scheme considered as success if both QSCs for control and target qubits perform a flawless error correction procedure simultaneously. Therefore, the upper-bound QBER performance of the QSC-protected two-qubit quantum gates, which is denoted as $\text{QBER}^{(2)}_{\text{upper}}$, can be determined by modifying Eq. (81) as follows:

$$\begin{aligned}\text{QBER}^{(2)}_{\text{upper}}(n,d,p) &= 1-\Big(1-\text{QBER}^{(1)}_{\text{upper}}(n,d,p)\Big)^2 \\ &= 1-\left(\sum_{i=0}^{t=\lfloor\frac{d-1}{2}\rfloor}\binom{n}{i}p^i(1-p)^{n-i}\right)^2.\end{aligned} \tag{90}$$

In this case, we assume that $p = p_f$ considering the errorneous stabilizer measurements, which is given by Eq. (75) for rotated-surface codes, surface codes, and toric codes, and by Eq. (78).

Similar to the case of transversal Hadamard gates, we also incorporate the formula of Eq. (82) for determining the lower-bound of the analytical QBER performance of the transversal CNOT gates protected by QSCs as follows:

$$\begin{aligned}\text{QBER}^{(2)}_{\text{upper}}(n,d,p) &= 1-\Big(1-\text{QBER}^{(1)}_{\text{lower}}(n,d,p)\Big)^2 \\ &= 1-\left(1-\sum_{i=0}^{t'+1}A(i)p^i(1-p)^{n-i}\right)^2\end{aligned} \tag{91}$$

given that $A(i)$ is a positive integer coefficient obeying

$$\sum_{i=0}^{t'+1}A_i \le 2^{(n-k)/2}, \text{ where } A_i=\binom{n}{i}. \tag{92}$$

Consequently, the final coefficient $A_{t'+1}$ is determined by

$$A_{t'+1} = 2^{(n-k)/2} - \sum_{i=0}^{t'}A_i. \tag{93}$$

In order to verify the analytical expression of Eq. (90), we have simulated the performance of QTECC-protected transversal CNOT gates protected by a distance-3 colour code, rotated-surface code, and surface code, exploiting the classical-to-quantum Pauli isomorphism. The results are depicted in Fig. 17. As expected, a similar trend to the QBER performance to the transversal Hadamard gates protected by QTECCs is displayed. An improvement in terms of QBER can be observed for depolarizing probabilities $p < 2 \times 10^{-3}$. Therefore, we conclude that our design in Fig. 6(b) indeed improves the reliability of both Hadamard gates as well as of CNOT gates.

Furthermore, we have plotted the upper-bound QBER analytical performance given in Eq. (90) for the transversal implementation of CNOT gates employing various types of QTECCs for different minimum distances d based on the code parameters of Table II. The corresponding QBER performance curves are portrayed in Fig. 18. We can also infer p_{th} values from Fig. 18, which defines the depolarizing probability value where we can start observing QBER improvements upon decreasing the quantum coding rate. Again, it also marks the QBER performance of the QSCs at the asymptotical limit. The p_{th} is represented by dashed lines in Fig. 18, where we have 2.61×10^{-3}, 2.71×10^{-3}, 1.26×10^{-3}, and 1.36×10^{-3}, respectively, for colour codes, rotated-surface codes, surface

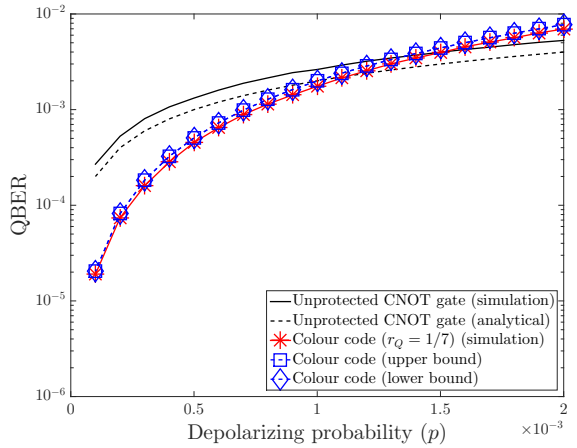

(a) Colour code.

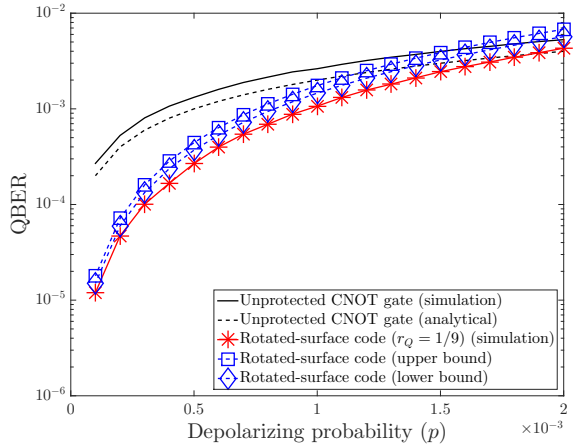

(b) Rotated-surface code.

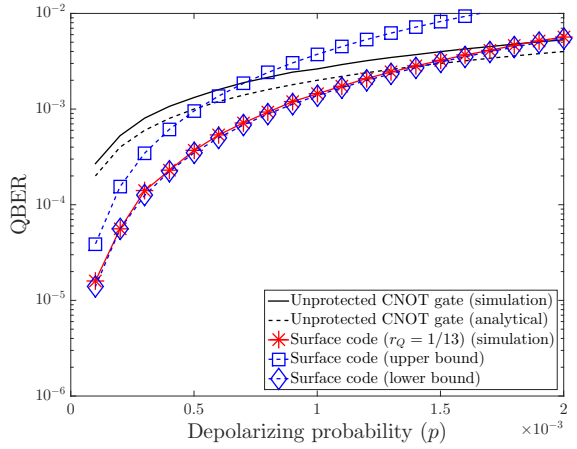

(c) Surface code.

Fig. 17: QBER performance for transversal configuration of CNOT gates protected by distance-3 QTECCs over quantum depolarizing channel. The quantum decoherence is inflicted after the transversal configuration of CNOT gates, where the error operators of $\prod_{i=1}^{c} P_i \in \mathcal{P}_n$ are defined by $p_i = p$. The number of consecutive error operators $c = 7$ for colour codes and $c = 5$ for surface and rotated-surface codes.

codes, and toric codes. Similarly, we have also plotted the lower-bound analytical QBER performance of the transversal CNOT gates protected by various QTECCs in Fig. 18 based on Eq. (91). In this case, we have the p_{th} values of 1.54×10^{-2}, 2.04×10^{-2}, 2.13×10^{-2}, and 2.17×10^{-2}, respectively, for colour, rotated-surface, surface, and toric codes.

Since the improvement in QBER domain can be clearly observed in Fig. 18, it is logical that the corresponding fidelity improvement can also be achieved. The essential question is what level of the fidelity the quantum gates have to be provided for ensuring that the QSC-protected quantum gates improve the overall fidelity of the system. Firstly, we have defined the output fidelity of the CNOT gates in Eq. (68), which is given below:

$$F_{\text{out}} = 1 - \text{QBER}_{\text{protected}}. \tag{94}$$

For asymptotical limit, based on Eq. (68), we can determine the threshold fidelity (F_{th}) as follows:

$$\begin{aligned} F_{\text{th}} &= 1 - 2p_{\text{th}} + p_{\text{th}}^2 \\ &\approx 1 - 2p_{\text{th}}, \end{aligned} \tag{95}$$

for $p_{\text{th}} \ll 1$. First, based on the upper-bound analytical QBER performance curves portrayed in Fig. 17, we can obtain the upper-bound F_{th} values required by each of the CNOT gates in order to gain the benefit of employing QSCs for protecting the transversal CNOT gates. By using Eq. (95), we have the upper-bound of the F_{th} values of 99.48%, 99.46%, 99.74%, and 99.72%, respectively, for colour codes, rotated-surface codes, surface codes, and toric codes. Additionally, based on Fig. 17, the lower-bound of the F_{th} can also be obtained using Eq. (95), where we have: 99.48%, 99.46%, 99.74%, and 99.72%,, respectively, for colour codes, rotated-surface codes, surface codes, and toric codes. All of the results presented in this subsection are summarized in Table III. Finally, we have shown that our framework proposed for protecting transversal quantum Clifford gates will provide a reliability improvement for both single-qubit and two-qubit quantum gates, provided that the fidelity threshold required for each of the quantum gates is satisfied.

VII. Conclusions and Future Works

A. Conclusions

We have presented a general framework for protecting quantum Clifford gates using QSCs along with the notion of the effective stabilizer formalism. In this treatise, we have also provided examples on how to utilize the advocated framework for protecting quantum Clifford gates. More specifically, in order to protect quantum Clifford gates, we arrange the gates in a transversal configuration in order to exploit the benefit of stabilizer operator preservation. Furthermore, since we considered imperfect quantum gates and also imperfect stabilizer measurements in our scheme, we invoked the QTECCs for correcting the errorneous physical qubits. The additional benefit of employing QTECCs is that the number of stabilizer measurements experienced by each of the physical qubits remains constant, as we increase the number of physical qubits. Hence, the spreading and propagation of

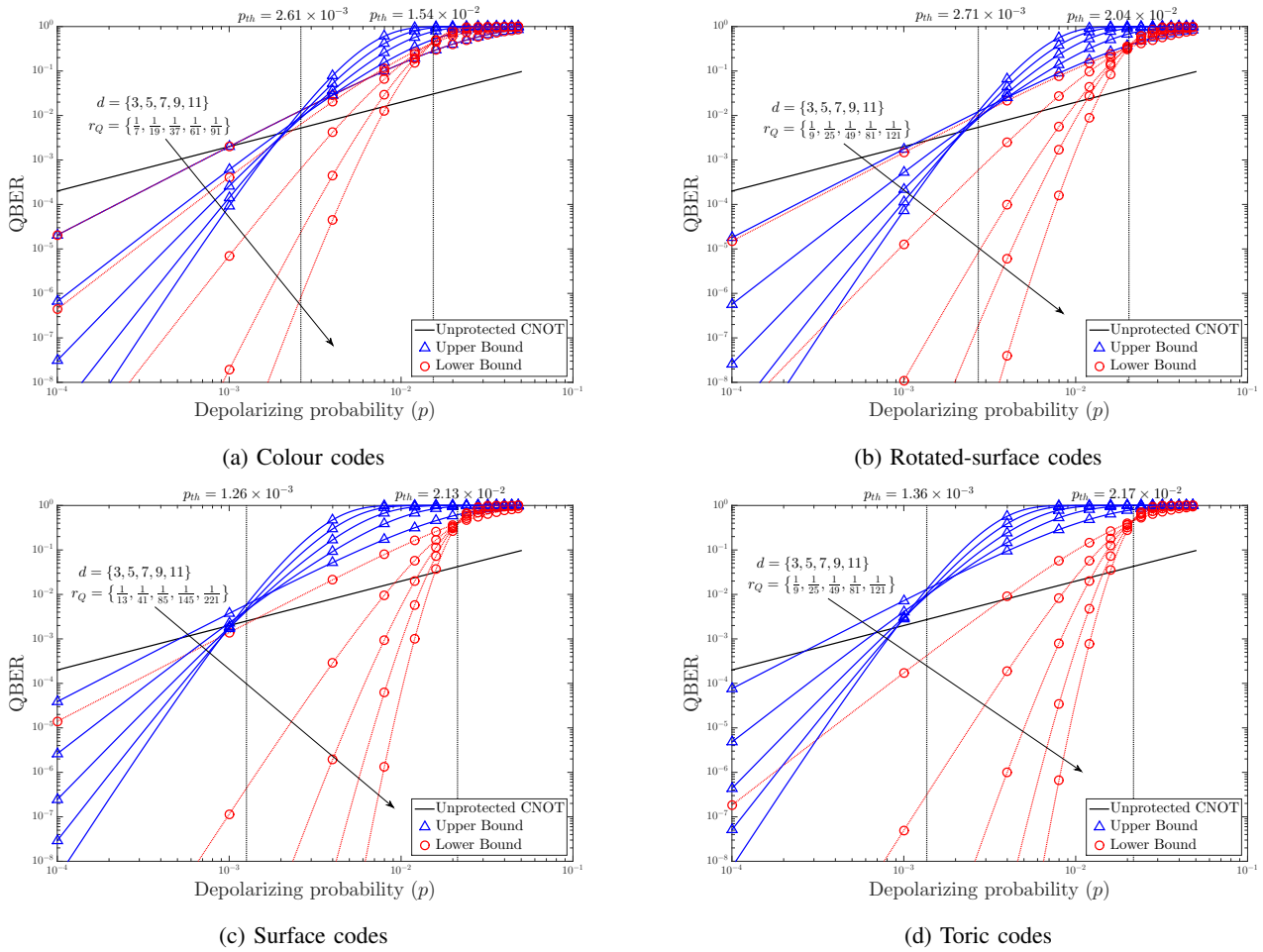

(a) Colour codes

(b) Rotated-surface codes

(c) Surface codes

(d) Toric codes

Fig. 18: Upper-bound and lower-bound analytical QBER performance curves of the transversal implementation of CNOT gates protected by QTECCs.

TABLE III: The summary of results of QTECC-protected transversal quantum Clifford gates.

Results	**Colour codes**	**Rotated-surface codes**	**Surface codes**	**Toric codes**
Upper bound p_{th} (error-free measurement)	1.83%	1.36%	0.63%	0.68%
Lower bound p_{th} (error-free measurement)	10.78%	10.20%	10.65%	10.85%
Upper bound p_{th} (with errorneous measurement)	0.26%	0.27%	0.13%	0.14%
Lower bound p_{th} (with errorneous measurement)	1.54%	2.04%	2.13%	2.17%
Upper bound F_{th} for Hadamard gates	99.74%	99.73%	99.87%	99.86%
Lower bound F_{th} for Hadamard gates	98.46%	97.96%	97.87%	97.83%
Upper bound F_{th} for CNOT gates	99.48%	99.46%	99.74%	99.72%
Lower bound F_{th} for CNOT gates	96.92%	95.92%	95.74%	95.66%

decoherence due to the interaction between qubits during stabilizer measurements can be effectively mitigated. We have shown that by combining the transversal implementation of quantum Clifford gates and the QTECCs, we can indeed improve the reliability of quantum Clifford gates, provided that they satisfy a minimum depolarization fidelity threshold F_{th}. In order to determine the approximate value of F_{th}, first we provide both the upper-bound and the lower-bound of the analytical QBER performance for both single-qubit and two-qubit transversal quantum gates protected by QSCs. Based on the upper-bound of the QBER performance, we obtain the critical F_{th} values for single-qubit quantum gates, which are as follows: 99.74%, 99.73%, 99.87%, and 99.86%, when protected by the colour, rotated-surface, surface, and toric codes, respectively. These F_{th} values were obtained at the asymptotical limit, namely when the number of physical

qubits is extremely large ($n \to \infty$) and the quantum coding rate tends to zero ($r_Q \to 0$). We need to emphasize that the upper-bound analytical QBER performance represents the worst-case scenario, where the error correction performance is purely defined by the minimum distance of the QSCs, whilst ignoring the potential advantage of exploiting the degeneracy property inhereted by QSCs. As a comparison, based on the lower-bound of the analytical QBER performance, we obtain the following F_{th} values for single-qubit quantum gates: 98.46%, 97.96%, 97.87%, and 97.83%, when protected by colour, rotated-surface, surface, and toric codes, respectively. By contrast, the lower-bound analytical QBER performance characterizes the optimistic scenario, where we assume that the degeneracy property inhereted by QTECCs can be exploited to approach the sphere-packing bound derived for non-degenerate QSCs.

By following the same line of investigation, we have also obtained the minimum depolarization fidelity threshold F_{th} values for two-qubit quantum gates, which is exemplified by CNOT gates in this treatise. The upper-bounds of the F_{th} values are given by, 99.48%, 99.46%, 99.74%, and 99.72%, respectively, when protected by colour, rotated-surface, surface, and toric codes, repectively. Similarly, the lower-bound of the F_{th} values are 96.92%, 95.92%, 95.74%, and 95.66%, respectively, when protected using colour, rotated-surface, surface, and toric codes. Ultimately, we believe that all the F_{th} values presented in this treatise mark the minimum fidelity requirement that has to be satisfied by the physical implementation of quantum gates, if we want to achieve the benefit of reliability improvement offered by QECCs for enhancing quantum computation.

B. Future Works

Our main goal with this treatise is to propose a general framework for protecting quantum gates utilizing QSCs. In deriving these preliminary results, we assume that each of the physical qubits experiences an individual and uncorrelated quantum depolarizing channel. Each of the quantum depolarizing channels is heavily characterized by the number of quantum gates interacting with the associated physical qubit. However, it is important to note that two-qubit quantum gates, such as a CNOT gate, potentially introduces error propagation between the physical qubits and therefore, it creates some level of correlation amongst the quantum depolarizing channels of each of the physical qubits. Hence, our next step is to include this correlation into our error model in order to get more realistic insights concerning the error correction performance of the proposed scheme.

We have exemplified the application of the framework for protecting transversal Hadamard and CNOT gates, which is equivalent to a single-step operation of Hadamard gates and CNOT gates. The natural extension of this work is to try to invoke the framework for much more complex circuits. Additionally, we have mentioned in this treatise that we only exploited the effective stabilizer formalism for transversal quantum Clifford gates. Therefore, combining the scheme conceived for the Clifford and non-Clifford gates indeed will create the universal set of quantum gates for quantum computation. Ultimately, our final goal is to construct a universal framework of protecting large-scale quantum computers using QECCs.

REFERENCES

[1] D. Gottesman, *Stabilizer codes and quantum error correction*. PhD thesis, California Institute of Technology, 1997.

[2] P. W. Shor, "Scheme for reducing decoherence in quantum computer memory," *Physical Review A*, vol. 52, no. 4, 1995.

[3] A. Steane, "Multiple-particle interference and quantum error correction," *Proceedings of the Royal Society of London A: Mathematical, Physical and Engineering Sciences*, vol. 452, no. 1954, pp. 2551–2577, 1996.

[4] A. M. Steane, "Error correcting codes in quantum theory," *Physical Review Letters*, vol. 77, no. 5, 1996.

[5] A. R. Calderbank and P. W. Shor, "Good quantum error-correcting codes exist," *Physical Review A*, vol. 54, no. 2, 1996.

[6] A. R. Calderbank, E. M. Rains, P. W. Shor, and N. J. Sloane, "Quantum error correction and orthogonal geometry," *Physical Review Letters*, vol. 78, no. 3, 1997.

[7] A. R. Calderbank, E. M. Rains, P. Shor, and N. J. Sloane, "Quantum error correction via codes over GF(4)," *IEEE Transactions on Information Theory*, vol. 44, no. 4, pp. 1369–1387, 1998.

[8] D. Poulin, J.-P. Tillich, and H. Ollivier, "Quantum serial turbo codes," *IEEE Transactions on Information Theory*, vol. 55, no. 6, pp. 2776–2798, 2009.

[9] Z. Babar, P. Botsinis, D. Alanis, S. X. Ng, and L. Hanzo, "The road from classical to quantum codes: A hashing bound approaching design procedure," *IEEE Access*, vol. 3, pp. 146–176, 2015.

[10] D. J. MacKay, G. Mitchison, and P. L. McFadden, "Sparse-graph codes for quantum error correction," *IEEE Transactions on Information Theory*, vol. 50, no. 10, pp. 2315–2330, 2004.

[11] Z. Babar, P. Botsinis, D. Alanis, S. X. Ng, and L. Hanzo, "Fifteen years of quantum LDPC coding and improved decoding strategies," *Access, IEEE*, vol. 3, pp. 2492–2519, 2015.

[12] M. M. Wilde and J. M. Renes, "Quantum polar codes for arbitrary channels," in *Proceedings of IEEE International Symposium on Information Theory (ISIT), 2012*, pp. 334–338, 2012.

[13] J. M. Renes, F. Dupuis, and R. Renner, "Efficient polar coding of quantum information," *Physical Review Letters*, vol. 109, no. 5, 2012.

[14] G. De Lange, Z. Wang, D. Riste, V. Dobrovitski, and R. Hanson, "Universal dynamical decoupling of a single solid-state spin from a spin bath," *Science*, vol. 330, no. 6000, pp. 60–63, 2010.

[15] T. Van der Sar, Z. Wang, M. Blok, H. Bernien, T. Taminiau, D. Toyli, D. Lidar, D. Awschalom, R. Hanson, and V. Dobrovitski, "Decoherence-protected quantum gates for a hybrid solid-state spin register," *Nature*, vol. 484, no. 7392, pp. 82–86, 2012.

[16] J. L. O'Brien, G. Pryde, A. Gilchrist, D. James, N. Langford, T. Ralph, and A. White, "Quantum process tomography of a controlled-NOT gate," *Physical Review Letters*, vol. 93, no. 8, 2004.

[17] A. Politi, M. J. Cryan, J. G. Rarity, S. Yu, and J. L. O'Brien, "Silica-on-silicon waveguide quantum circuits," *Science*, vol. 320, no. 5876, pp. 646–649, 2008.

[18] L. DiCarlo, J. Chow, J. Gambetta, L. Bishop, B. Johnson, D. Schuster, J. Majer, A. Blais, L. Frunzio, S. Girvin, *et al.*, "Demonstration of two-qubit algorithms with a superconducting quantum processor," *Nature*, vol. 460, no. 7252, p. 240, 2009.

[19] J. M. Chow, J. M. Gambetta, A. Córcoles, S. T. Merkel, J. A. Smolin, C. Rigetti, S. Poletto, G. A. Keefe, M. B. Rothwell, J. Rozen, *et al.*, "Universal quantum gate set approaching fault-tolerant thresholds with superconducting qubits," *Physical Review Letters*, vol. 109, no. 6, 2012.

[20] M. Veldhorst, J. Hwang, C. Yang, A. Leenstra, B. De Ronde, J. Dehollain, J. Muhonen, F. Hudson, K. M. Itoh, A. Morello, *et al.*, "An addressable quantum dot qubit with fault-tolerant control-fidelity," *Nature Nanotechnology*, vol. 9, no. 12, pp. 981–985, 2014.

[21] M. Veldhorst, C. Yang, J. Hwang, W. Huang, J. Dehollain, J. Muhonen, S. Simmons, A. Laucht, F. Hudson, K. Itoh, *et al.*, "A two-qubit logic gate in silicon," *Nature*, vol. 526, no. 7573, pp. 410–414, 2015.

[22] C. Ballance, T. Harty, N. Linke, M. Sepiol, and D. Lucas, "High-fidelity quantum logic gates using trapped-ion hyperfine qubits," *Physical review letters*, vol. 117, no. 6, 2016.

[23] H. V. Nguyen, Z. Babar, D. Alanis, P. Botsinis, D. Chandra, S. X. Ng, and L. Hanzo, "EXIT-chart aided quantum code design improves the normalised throughput of realistic quantum devices," *IEEE Access*, vol. 4, pp. 10194–10209, 2016.

[24] E. Knill, R. Laflamme, and W. H. Zurek, "Resilient quantum computation: Error models and thresholds," *Proceedings of the Royal Society of London A: Mathematical, Physical and Engineering Sciences*, vol. 454, no. 1969, pp. 365–384, 1998.

[25] J. Preskill, "Reliable quantum computers," *Proceedings of the Royal Society of London A: Mathematical, Physical and Engineering Sciences*, vol. 454, no. 1969, pp. 385–410, 1998.

[26] S. Bravyi and A. Kitaev, "Universal quantum computation with ideal Clifford gates and noisy ancillas," *Physical Review A*, vol. 71, no. 2, 2005.

[27] D. Aharonov and M. Ben-Or, "Fault-tolerant quantum computation with constant error rate," *SIAM Journal on Computing*, 2008.

[28] H. Bombín, "Single-shot fault-tolerant quantum error correction," *Physical Review X*, vol. 5, no. 3, 2015.

[29] O. Fawzi, A. Grospellier, and A. Leverrier, "Constant overhead quantum fault-tolerance with quantum expander codes," in *Proceedings of 59th IEEE Annual Symposium on Foundations of Computer Science (FOCS), 2018*, pp. 743–754, IEEE, 2018.

[30] E. Campbell, "A theory of single-shot error correction for adversarial noise," *Quantum Science and Technology*, vol. 4, no. 2, 2019.

[31] T. Jochym-O'Connor, "Fault-tolerant gates via homological product codes," *Quantum*, vol. 3, 2019.

[32] A. Y. Kitaev, "Quantum computations: Algorithms and error correction," *Russian Mathematical Surveys*, vol. 52, no. 6, pp. 1191–1249, 1997.

[33] S. B. Bravyi and A. Y. Kitaev, "Quantum codes on a lattice with boundary," *arXiv preprint quant-ph/9811052*, 1998.

[34] H. Bombin and M. A. Martin-Delgado, "Topological quantum distillation," *Physical Review Letters*, vol. 97, no. 18, 2006.

[35] C. Horsman, A. G. Fowler, S. Devitt, and R. Van Meter, "Surface code quantum computing by lattice surgery," *New Journal of Physics*, vol. 14, no. 12, 2012.

[36] S. Bravyi and B. Terhal, "A no-go theorem for a two-dimensional self-correcting quantum memory based on stabilizer codes," *New Journal of Physics*, vol. 11, no. 4, 2009.

[37] S. Bravyi, D. Poulin, and B. Terhal, "Tradeoffs for reliable quantum information storage in 2D systems," *Physical Review Letters*, vol. 104, no. 5, 2010.

[38] D. Chandra, Z. Babar, H. V. Nguyen, D. Alanis, P. Botsinis, S. X. Ng, and L. Hanzo, "Quantum topological error correction codes: The classical-to-quantum isomorphism perspective," *IEEE Access*, 2017.

[39] Y. Fujiwara, "Ability of stabilizer quantum error correction to protect itself from its own imperfection," *Physical Review A*, vol. 90, no. 6, 2014.

[40] A. Ashikhmin, C.-Y. Lai, and T. A. Brun, "Robust quantum error syndrome extraction by classical coding," in *IEEE International Symposium on Information Theory, 2014*, pp. 546–550, IEEE, 2014.

[41] A. Ashikhmin, C.-Y. Lai, and T. A. Brun, "Correction of data and syndrome errors by stabilizer codes," in *IEEE International Symposium on Information Theory (ISIT), 2016*, pp. 2274–2278, IEEE, 2016.

[42] W. Zeng, A. Ashikhmin, M. Woolls, and L. P. Pryadko, "Quantum convolutional data-syndrome codes," *arXiv preprint arXiv:1902.07395*, 2019.

[43] A. Ashikhmin, C.-Y. Lai, and T. A. Brun, "Quantum data-syndrome codes," *arXiv preprint arXiv:1907.01393*, 2019.

[44] Z. Babar, D. Chandra, H. V. Nguyen, P. Botsinis, D. Alanis, S. X. Ng, and L. Hanzo, "Duality of Quantum and Classical Error Correction Codes: Design Principles and Examples," *IEEE Communications Surveys & Tutorials*, vol. 21, no. 1, pp. 970–1010, 2018.

[45] D. A. Lidar and T. A. Brun, *Quantum Error Correction*. Cambridge University Press, 2013.

[46] M. A. Nielsen and I. L. Chuang, *Quantum Computation and Quantum Information*. Cambridge University Press, 2000.

[47] P. A. Dirac, "A new notation for quantum mechanics," *Proceedings of the Cambridge Philosophical Society*, vol. 35, pp. 416–418, 1939.

[48] P. W. Shor, "Algorithms for quantum computation: Discrete logarithms and factoring," in *Proceedings of 35th Annual Symposium on Foundations of Computer Science, 1994*, pp. 124–134, 1994.

[49] P. W. Shor, "Polynomial-time algorithms for prime factorization and discrete logarithms on a quantum computer," *SIAM Review*, vol. 41, no. 2, pp. 303–332, 1999.

[50] L. K. Grover, "A fast quantum mechanical algorithm for database search," in *Proceedings of 28th Annual ACM Symposium on Theory of Computing, 1996*, pp. 212–219, 1996.

[51] L. K. Grover, "Quantum mechanics helps in searching for a needle in a haystack," *Physical Review Letters*, vol. 79, no. 2, 1997.

[52] D. E. Deutsch, "Quantum computational networks," *Proceedings of the Royal Society of London A: Mathematical, Physical and Engineering Sciences*, vol. 425, no. 1868, pp. 73–90, 1989.

[53] R. Raussendorf, D. E. Browne, and H. J. Briegel, "Measurement-based quantum computation on cluster states," *Physical Review A*, vol. 68, no. 2, 2003.

[54] G. Grössing and A. Zeilinger, "Quantum cellular automata," *Complex Systems*, vol. 2, no. 2, pp. 197–208, 1988.

[55] M. Freedman, A. Kitaev, M. Larsen, and Z. Wang, "Topological quantum computation," *Bulletin of the American Mathematical Society*, vol. 40, no. 1, pp. 31–38, 2003.

[56] E. Farhi, J. Goldstone, S. Gutmann, and M. Sipser, "Quantum computation by adiabatic evolution," *arXiv preprint quant-ph/0001106*, 2000.

[57] R. Cleve and D. Gottesman, "Efficient computations of encodings for quantum error correction," *Physical Review A*, vol. 56, no. 1, 1997.

[58] M. Grassl, "Variations on encoding circuits for stabilizer quantum codes," in *Proceedings of International Conference on Coding and Cryptology, 2011*, pp. 142–158, Springer, 2011.

[59] I. Djordjevic, *Quantum Information Processing and Quantum Error Correction: An Engineering Approach*. Academic press, 2012.

[60] D. Chandra, Z. Babar, H. V. Nguyen, D. Alanis, P. Botsinis, S. X. Ng, and L. Hanzo, "Quantum coding bounds and a closed-form approximation of the minimum distance versus quantum coding rate," *IEEE Access*, vol. 5, pp. 11557–11581, 2017.

[61] P. Botsinis, Z. Babar, D. Alanis, D. Chandra, H. Nguyen, S. X. Ng, and L. Hanzo, "Quantum error correction protects quantum search algorithms against decoherence," *Scientific Reports*, vol. 6, 2016.

[62] S. J. Devitt, W. J. Munro, and K. Nemoto, "Quantum error correction for beginners," *Reports on Progress in Physics*, vol. 76, no. 7, 2013.

[63] J. Łodyga, P. Mazurek, A. Grudka, and M. Horodecki, "Simple scheme for encoding and decoding a qubit in unknown state for various topological codes," *Scientific Reports*, vol. 5, 2015.

[64] D. Gottesman, "The Heisenberg representation of quantum computers," *arXiv preprint quant-ph/9807006*, 1998.

[65] S. Aaronson and D. Gottesman, "Improved simulation of stabilizer circuits," *Physical Review A*, vol. 70, no. 5, 2004.

[66] P. W. Shor, "Fault-tolerant quantum computation," in *Proceedings of 37th Annual Symposium on Foundations of Computer Science, 1996*, pp. 56–65, 1996.

[67] E. Knill, R. Laflamme, and W. H. Zurek, "Resilient quantum computation," *Science*, vol. 279, no. 5349, pp. 342–345, 1998.

[68] A. M. Steane, "Space, time, parallelism and noise requirements for reliable quantum computing," *Fortschritte der Physik*, vol. 46, no. 4-5, pp. 443–457, 1998.

[69] D. Gottesman, "Theory of fault-tolerant quantum computation," *Physical Review A*, vol. 57, no. 1, 1998.

[70] A. M. Steane, "Overhead and noise threshold of fault-tolerant quantum error correction," *Physical Review A*, vol. 68, no. 4, 2003.

[71] H. Bombin and M. A. Martin-Delgado, "Quantum measurements and gates by code deformation," *Journal of Physics A: Mathematical and Theoretical*, vol. 42, no. 9, 2009.

[72] H. Bombin, "Clifford gates by code deformation," *New Journal of Physics*, vol. 13, no. 4, 2011.

[73] J. T. Anderson, G. Duclos-Cianci, and D. Poulin, "Fault-tolerant conversion between the Steane and Reed-Muller quantum codes," *Physical review letters*, vol. 113, no. 8, 2014.

[74] C. Vuillot, L. Lao, B. Criger, C. G. Almudever, K. Bertels, and B. Terhal, "Code deformation and lattice surgery are gauge fixing," *New Journal of Physics*, vol. 21, no. 3, 2019.

[75] A. G. Fowler, A. M. Stephens, and P. Groszkowski, "High-threshold universal quantum computation on the surface code," *Physical Review A*, vol. 80, no. 5, 2009.

[76] D. S. Wang, A. G. Fowler, and L. C. Hollenberg, "Surface code quantum computing with error rates over 1%," *Physical Review A*, vol. 83, no. 2, 2011.

[77] A. G. Fowler, M. Mariantoni, J. M. Martinis, and A. N. Cleland, "Surface codes: Towards practical large-scale quantum computation," *Physical Review A*, vol. 86, no. 3, 2012.

[78] T. A. Brun, Y.-C. Zheng, K.-C. Hsu, J. Job, and C.-Y. Lai, "Teleportation-based fault-tolerant quantum computation in multi-qubit large block codes," *arXiv preprint arXiv:1504.03913*, 2015.

[79] R. Jozsa, "Fidelity for mixed quantum states," *Journal of Modern Optics*, vol. 41, no. 12, pp. 2315–2323, 1994.

[80] B. Schumacher, "Quantum coding," *Physical Review A*, vol. 51, no. 4, 1995.

[81] E. Knill and R. Laflamme, "Theory of quantum error-correcting codes," *Physical Review A*, vol. 55, no. 2, 1997.

[82] A. J. Landahl, J. T. Anderson, and P. R. Rice, "Fault-tolerant quantum computing with color codes," *arXiv preprint arXiv:1108.5738*, 2011.
[83] F. J. MacWilliams and N. J. A. Sloane, *The theory of error-correcting codes*. Elsevier, 1977.
[84] J. I. Hall, *Notes on coding theory*. FreeTechBooks, 2003.

Daryus Chandra (S'15) received the M.Eng. degree in electrical engineering from Universitas Gadjah Mada, Indonesia, in 2014. He is currently pursuing the Ph.D. degree with the Next Generation Wireless ResearchGroup, School of Electronics and Computer Science, University of Southampton, UK. He is a recipient of scholarship award from the Indonesia Endowment Fund for Education (Lembaga Pengelola Dana Pendidikan, LPDP).

His research interests include classical and quantum error correction codes, quantum information, and quantum communications.

Zunaira Babar received her B.Eng. degree in electrical engineering from the National University of Science & Technology (NUST), Islamabad, Pakistan, in 2008, and the M.Sc. degree (Distinction) and the Ph.D degree in wireless communications from the University of Southampton, UK, in 2011 and 2015, respectively.

Her research interests include quantum error correction codes, channel coding, coded modulation, iterative detection and cooperative communications.

Hung Viet Nguyen received the B.Eng. degree in Electronics & Telecommunications from Hanoi University of Science and Technology (HUST), Hanoi, Vietnam, in 1999, the M.Eng. in Telecommunications from Asian Institute of Technology (AIT), Bangkok, Thailand, in 2002 and the Ph.D. degree in wireless communications from the University of Southampton, Southampton, U.K., in 2013. Since 1999 he has been a lecturer at the Post & Telecommunications Institute of Technology (PTIT), Vietnam. He is involved in the OPTIMIX and CONCERTO European projects. He is currently a postdoctoral researcher at Southampton Wireless (SW) group, University of Southampton, UK.

His research interests include cooperative communications, channel coding, network coding, and quantum communications.

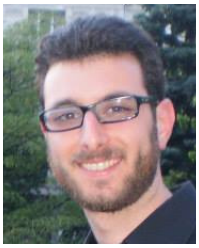

Dimitrios Alanis (S'13) received the M.Eng. degree in Electrical and Computer Engineering from the Aristotle University of Thessaloniki in 2011 and the M.Sc. and PhD degrees in Wireless Communications from the University of Southampton in 2012 and 2017, respectively. He is currently working as a Research Fellow in Southampton Wireless (SW) group, School of Electronics and Computer Science of the University of Southampton, UK.

His research interests include quantum computation and quantum information theory, quantum search algorithms, cooperative communications, resource allocation for self-organizing networks, bio-inspired optimization algorithms and classical and quantum game theory.

Panagiotis Botsinis (S'12-M'16) received the M.Eng. degree from the School of Electrical and Computer Engineering of the National Technical University of Athens (NTUA), Greece, in 2010, as well as the M.Sc. degree with distinction and the Ph.D. degree in Wireless Communications from the University of Southampton, UK, in 2011 and 2015, respectively. He is currently working as a Research Fellow in the Southampton Wireless group at the School of Electronics and Computer Science of the University of Southampton, UK. Since October 2010, he has been a member of the Technical Chamber of Greece.

His research interests include quantum-assisted communications, quantum computation, iterative detection, OFDM, MIMO, multiple access systems, coded modulation, channel coding, cooperative communications, as well as combinatorial optimization.

Soon Xin Ng (S'99-M'03-SM'08) received the B.Eng. degree (First class) in electronic engineering and the Ph.D. degree in telecommunications from the University of Southampton, Southampton, U.K., in 1999 and 2002, respectively. From 2003 to 2006, he was a postdoctoral research fellow working on collaborative European research projects known as SCOUT, NEWCOM and PHOENIX. Since August 2006, he has been a member of academic staff in the School of Electronics and Computer Science, University of Southampton. He is involved in the OPTIMIX and CONCERTO European projects as well as the IU-ATC and UC4G projects. He is currently an Associate Professor in telecommunications at the University of Southampton.

His research interests include adaptive coded modulation, coded modulation, channel coding, space-time coding, joint source and channel coding, iterative detection, OFDM, MIMO, cooperative communications, distributed coding, quantum error correction codes and joint wireless-and-optical-fibre communications. He has published over 200 papers and co-authored two John Wiley/IEEE Press books in this field. He is a Senior Member of the IEEE, a Chartered Engineer and a Fellow of the Higher Education Academy in the UK.

Lajos Hanzo (M'91-SM'92-F'04) received his degree in electronics in 1976 and his doctorate in 1983. In 2009 he was awarded the honorary doctorate "Doctor Honoris Causa" by the Technical University of Budapest. During his 38-year career in telecommunications he has held various research and academic posts in Hungary, Germany and the UK. Since 1986 he has been with the School of Electronics and Computer Science, University of Southampton, UK, where he holds the chair in telecommunications. He has successfully supervised 112 PhD students, co-authored 18 John Wiley/IEEE Press books on mobile radio communications totalling in excess of 10 000 pages, published 1692 research contributions at IEEE Xplore, acted both as TPC and General Chair of IEEE conferences, presented keynote lectures and has been awarded a number of distinctions. Currently he is directing a 100-strong academic research team, working on a range of research projects in the field of wireless multimedia communications sponsored by industry, the Engineering and Physical Sciences Research Council (EPSRC) UK, the European Research Councils Advanced Fellow Grant and the Royal Societys Wolfson Research Merit Award. He is an enthusiastic supporter of industrial and academic liaison and he offers a range of industrial courses.

Lajos is a Fellow of the Royal Academy of Engineering, of the Institution of Engineering and Technology, and of the European Association for Signal Processing. He is also a Governor of the IEEE VTS. During 2008–2012 he was the Editor-in-Chief of the IEEE Press and a Chaired Professor also at Tsinghua University, Beijing. He has 30 000+ citations. For further information on research in progress and associated publications please refer to http://www.wireless.ecs.soton.ac.uk.